RSC Advances

PAPER

View Article Online
View Journal | View Issue

Cite this: *RSC Adv.*, 2023, **13**, 24955

Annealing-induced phase transformation in $In_{10}Se_{70}Te_{20}$ thin films and its structural, optical and morphological changes for optoelectronic applications†

Sasmita Giri,[a] P. Priyadarshini,[a] D. Alagarasan,[bc] R. Ganesan[c] and R. Naik *[a]

In_2Se_3 and In_2Te_3 have great importance in various device fabrications. The present report is based on the annealing-induced phase formation of both In_2Se_3 and In_2Te_3 from $In_{10}Se_{70}Te_{20}$ thin films at different annealing temperatures as found from the XRD analysis and well supported by the Raman study. The average crystallite size increased with a decrease in the dislocation density. The surface morphology changed with annealing and increased in particle size as noticed from the FESEM images. The uniform distribution and presence of constituent elements in the film were verified using EDX data. The increase in transmittance is accompanied by a decrease in extinction coefficient, optical density and increase in skin depth with annealing. The increase in optical bandgap from 0.418 eV to 0.645 eV upon annealing at 250 °C is associated with a decrease in disorder. The steepness parameter increased and the S_{e-p} value decreased with annealing. The refractive index decreased with an increase in oscillator energy and decrease in dispersion energy. The quality factor, dielectric loss, optical conductivity and electrical susceptibility decreased. The optical electronegativity and plasma frequency increased with annealing. There is a significant change in the non-linear susceptibility and non-linear refractive index with annealing. The observed changes in the film structure and optical behaviour are due to the annealing-induced phase formation from the $In_{10}Se_{70}Te_{20}$ host matrix upon annealing. Such materials are suitable for optoelectronic and phase change devices.

Received 4th June 2023
Accepted 9th August 2023

DOI: 10.1039/d3ra03731b

rsc.li/rsc-advances

1. Introduction

The large transparency window in IR regions by Te- and Se-doped chalcogenide films is important owing to their applications in phase change memory devices, photodetectors, photovoltaics, solar cells, infrared detectors, *etc.*[1–5] Se-based materials are used for imaging and biomedical applications, whereas Te-based materials are used for infrared detectors and phase-change memory devices.[6] Se-based chalcogenide compounds possess high transmission ability in the mid and far IR range and possess strong non-linearity.[7] Se-based materials have advantages such as low melting point, low thermal conductivity, and stability, and they possess the property of easy formation of compounds with doping elements.[8,9] Similarly, Te has unique properties for cutting-edge technologies with chalcogenides.[10] The high transmittance in the far infra-red regime is used for IR optics and optical fibers.[11,12] The ultrafast crystallization of Te-based materials is used in phase change optical data storage devices.[13–16] Binary compounds based on Te–Se alloys have been studied widely because they have fast access to information, great storage capacity, and electro photographic applications, such as laser printing and photoreceptors in photocopying.[17,18] Se–Te binary compounds have more advantages than pure Se because of their greater hardness, high photosensitivity, higher crystallization temperature, and low aging effects. The thin film forms of Se–Te compounds are promising owing to their wide applications.[19] Se–Te alloys are prime candidates for thermoelectric power, and many semiconducting chalcogenide compounds have been reported for the direct energy conversion of thermal to electrical energy.[20,21] Thermally evaporated Se_xTe_{1-x} thin films with tuneable energy gaps are used for high-performance SWIR photodetector fabrication.[2] The additive of metallic components to the Se–Te matrix has led to high thermal stability.[17] The introduction of In into either Te or Se is very attractive for various applications.

In_2Te_3 is a layer III–IV type material that is sensitive to strain and pressure and is used for superconductor applications.[22] The α-In_2Te_3 films have stable photo switching ability ranging from 370–1064 nm with a short response time of 15 ms. The good

[a]*Department of Engineering and Material Physics, ICT-IOC, Bhubaneswar, 751013, India. E-mail: ramakanta.naik@gmail.com*

[b]*Nitte Meenakshi Institute of Technology, Yelahanka, Bengaluru, 560064, India*

[c]*Department of Physics, Indian Institute of Science, Bangalore, 560012, India*

† Electronic supplementary information (ESI) available. See DOI: https://doi.org/10.1039/d3ra03731b

figure-of-merit, stability and broad spectral range of α-In_2Te_3 are used for next-generation photo detectors.[23] In_2Te_3 is having a direct band gap of ~1.1 eV with a high absorption coefficient value of over 500–2500 nm, which makes it a suitable absorber layer in photovoltaic cells.[24,25]

Similarly, In_2Se_3 has shown attractive properties and great potential in the applications of ferroelectric devices.[26] The leveraging of the semiconducting and ferroelectricity nature of α-In_2Se_3 and ferroelectric semiconductor field-effect transistors (FeSFETs) are made for neuromorphic instruments for brain-inspired intelligent systems.[27] The β-In_2Se_3 nanosheets are a type of indirect band gap semiconductors with E_g of ~1.55 eV. Single nanosheet photodetectors possess fast response times and high photoresponsivity.[28] The facile integration, patterning, and packaging of high-quality 2D chalcogenide In_2Se_3 are used for wearable electronics, next-generation photodetector arrays, and integrated optoelectronic circuits.[29] However, ternary compounds with In–Se–Te are of great importance in research.

In–Se–Te-based ternary alloys have various structural changes, such as β and α phases, and vacant of In sub-lattices for one-third or two-third for other dopant impurities. Therefore, the appearance of the In–Se and In–Te phases from the phase diagram infers the formation of In_2Se_3 and In_2Te_3 phases. Among them, indium-doped Se–Te alloys have found great importance in various devices because of their enhanced optical properties.[30] Elkatlawy *et al.* prepared $Se_{80}Te_{20-x}In_x$ thin films with different compositions and revealed that In doping $Se_{80}Te_{20-x}In_x$ improved the transmittance range and refractive index in visible and near IR regions.[31] Saxena *et al.* reported an increase in thermal conductivity and thermal diffusivity in $Se_{80}Te_{20-x}In_x$ bulk with indium addition.[32] Se–Te–In ternary compounds have wide applications in photoreceptors, optical recording media, xerography, infrared spectroscopy, and laser fiber techniques.[33,34] Such ternary compounds under different energy treatments, such as laser irradiation, ion irradiation, thermal annealing, proton and irradiation, show profound property modifications, which are useful for many applications.[35–38]

The In_2Se_3 band gap is found to be reduced by annealing for the increase in the width of localized states near the band edges. The change in film density reduced the transmittance and increased the absorption, making it suitable for solar cell applications.[39] The reduction in the band gap in $Se_{75-x}Te_{25}In_x$ with annealing is a good one because of the material to be used in optical storage.[40] Thermal annealing on $Se_{80}Te_{20-x}In_x$ thin films changed the structure from amorphous to crystalline with annealing temperature and an increase in refractive index with a reduction in bandgap with annealing time duration.[41] By considering the importance of thermal annealing, this study is based on the thermal annealing of $In_{10}Se_{70}Te_{20}$ thin films at various temperatures.

The prime objective of the study is to observe (i) the thermal annealing-induced structural changes in $In_{10}Se_{70}Te_{20}$ thin films at various annealing temperatures, (ii) the change in linear-nonlinear optical properties and (iii) morphological changes due to phase transformation in the films. The prepared film samples were thermally annealed at the following temperatures: 100, 150, 200, and 250 °C. X-ray diffraction (XRD) confirms the structural properties, which are strongly corroborated by performing Raman analysis. Field emission scanning electron microscopy (FESEM) was used for the surface morphology imaging. The composition of the films was confirmed by energy dispersive X-ray analysis (EDX). The optical parameters of the annealed $In_{10}Se_{70}Te_{20}$ thin films were analysed using UV-Visible spectroscopy.

2. Experimental

2.1. Thin film preparation

The bulk $In_{10}Se_{70}Te_{20}$ samples were prepared using high pure In, Se, Te (Sigma Aldrich, 99.999%) elements by applying the melt quenching method. The required chemical amounts were sealed at a vacuum of 10^{-5} Torr inside the quartz ampoule and placed inside a furnace at 500 °C for 30 h. The melt formed inside the ampoule was quenched rapidly in liquid nitrogen to obtain the bulk $In_{10}Se_{70}Te_{20}$ sample. From the prepared bulk sample, $In_{10}Se_{70}Te_{20}$ thin films were deposited by employing the thermal evaporation method using an HHV (Smart Coat 3) vacuum coating unit.

About 800 nm thickness of $In_{10}Se_{70}Te_{20}$ thin films was deposited on clean substrates (corning glass) at a rate of 5 Å per second. During the whole deposition process, the pressure inside the deposition chamber was maintained at ~5×10^{-5} Torr, and the substrate temperature was kept at room temperature. The substrate holder was rotated slowly to obtain a homogeneous and uniform film. The film thickness was controlled by the filament current using the current-controlling unit. A crystal sensor is fixed in the deposition chamber to measure the film thickness, which is recorded and displayed on the digital thickness monitor. The thin films were annealed for 1.5 hours at 100, 150, 200, and 250 °C in a hot air oven.

2.2. Characterization

The structural properties were studied using a Bruker D8 Advance XRD unit with Cu K_α-radiation of wavelength λ = 1.5418 Å. The XRD data were recorded with a step size of 0.02° s^{-1} for the range from $2\theta = 10°$ to 70°. The change in vibrational mode was determined from Raman spectroscopy (LabRAM HR system) using a 532 nm argon laser source with a CCD detector in backscattering mode. The spectra were recorded from the 50–400 cm^{-1} range. The spectra calibration was done using the silicon 520 cm^{-1} line, and 3–4 measurements were taken after calibration at different positions for the same time intervals (40 seconds) to minimize the systematic error. Furthermore, the morphology was imaged using an FESEM (JEOL-JSM-7610F) unit, and the ratio of elemental composition was observed from the EDX unit attached to the FESEM unit. The imaging was done at a voltage of 20 kV during the characterization process.

The transmittance and absorbance spectra of as-prepared and annealed $In_{10}Se_{70}Te_{20}$ thin films were recorded from the JASCO V-770 UV-Visible spectrophotometer in the wavelength range of 500–2500 nm. The linear and non-linear optical

properties were calculated from the transmission data using various relations.

3. Results and discussion

3.1. Structural study by XRD and Raman spectroscopy

The XRD pattern of $In_{10}Se_{70}Te_{20}$ (as-prepared and annealed) thin films is shown in Fig. 1a, which confirms the crystalline nature with the appearance of In_2Te_3, In_4Se_3, and In_4Te_3 phases in the films. The as-prepared film showed crystalline peaks at 23.95° (5 1 1) and 41.13° (8 2 2), corresponding to the cubic phase of In_2Te_3 phase (ICSD: 33-1488) and a peak at 29.46° (0 4 0) representing the orthorhombic In_4Se_3 phase (ICDS: 48-1575). Among these three crystalline peaks, the former two peaks remain intact with intensity and position. However, the peak intensity of the In_4Se_3 peak becomes more intense and prominent with annealing, which is possibly due to thermal energy through annealing. Furthermore, annealing of the $In_{10}Se_{70}Te_{20}$ thin films results in the appearance of additional peaks at 23.41° (0 1 1) and 48.56° (8 0 0), corresponding to the same orthorhombic In_4Se_3 phase (ICDS: 48-1575). The crystalline peaks at 28.76° (3 1 1), 44.65° (3 5 1), and 51.11° (7 3 1) present the orthorhombic In_4Te_3 phase (ICDS: 01-071-2085), respectively. It is noteworthy that the intensity, peak number, and sharpness of the peaks are enhanced with annealing, which ensures increased crystallinity through the formation of large crystallites, as confirmed by several studies.[42,43] The formation of more binary In-chalcogen phases might be due to the sufficient kinetic energy of indium, which allows more diffusion of indium with chalcogen lattices (here selenium and tellurium), with annealing temperature and forms bonds with Se and Te atoms.[44] In other words, the defects and unsaturated bonds are annealed out by forming many saturated bonds at boundaries with an increased annealing temperature. Such bonds cause structural variation in annealed $In_{10}Se_{70}Te_{20}$ films.

Based on the XRD pattern, the average crystallite size (D) calculated from the full-width half maxima (FWHM) observed prominent peaks using Scherer's equation:[45]

$$\text{Crystallite size } (D) = \frac{0.9\lambda}{\beta \cos\theta}, \quad (1)$$

where 'λ' is the Cu K_α-line wavelength (1.54 Å), θ is the incidence angle, and β is the FWHM that infers the structural broadening. The δ (dislocation density), ε (lattice strain), and the number of crystallites per unit surface area (N_c) were evaluated using the following equations:[46]

$$\text{Lattice strain } (\varepsilon) = \frac{\beta \cot\theta}{4}, \quad (2)$$

$$\text{Dislocation density } (\delta) = \frac{1}{D^2}, \; N_c = \frac{t}{D^3}, \quad (3)$$

where t has a value of ~800 nm (film thickness). The evaluated structural parameters for the different films are presented in Table 1. The 'D' value increased with annealing for the coalescence of smaller grains. The formed In_2Te_3 and In_4Se_3 crystalized phases in the as-prepared film possibly act as nucleation points for the heterogeneous growth of other phases at different annealing temperatures.[47] Simultaneously, the δ and ε values decreased, confirming the increase in crystallinity with annealing. The +ve value of residual strain implies that the tensile strain in the film developed owing to the difference in the thermal expansion coefficient of the deposited film and substrate. The N_c value decreased with annealing temperature because of the change in structure for the coalescence of smaller crystallites.[48]

Table 1 Structural parameters of $In_{10}Se_{70}Te_{20}$ thin films

Structural parameters	D (nm)	$\delta \times 10^{15}$ (m^{-2})	ε	N_C (nm^{-2})
As-prepared	9.55	0.0109	0.014	0.91
Annl 100 °C	12.90	0.0060	0.011	0.37
Annl 150 °C	13.17	0.0057	0.010	0.35
Annl 200 °C	14.43	0.0047	0.008	0.26
Annl 250 °C	18.68	0.0028	0.005	0.12

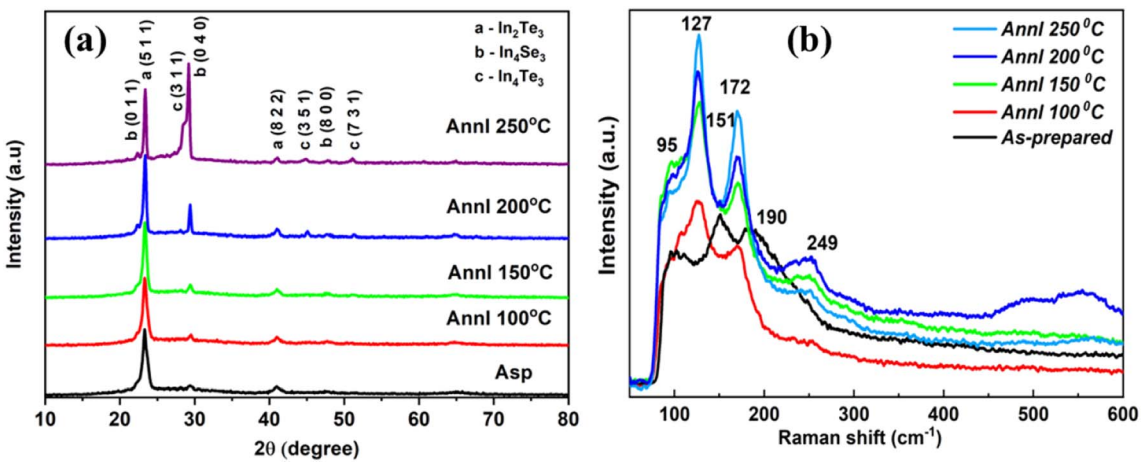

Fig. 1 (a) XRD pattern and (b) Raman spectra of $In_{10}Se_{70}Te_{20}$ thin films.

Raman spectroscopic analysis is an effective method for studying the structural aspects of non-crystalline compounds. The nature of the chemical bonds, atomic arrangements, and structural changes in vibrational levels induced by external energy were viewed through Raman analysis. The Raman data of $In_{10}Se_{70}Te_{20}$ thin film are presented in Fig. 1b, which depicts different peaks ranging from 50 to 600 cm^{-1} for the as-prepared and annealed films. The as-deposited $In_{10}Se_{70}Te_{10}$ thin film has peaks at 95, 151, and 190 cm^{-1}, corresponding to the In–Se phase.[49–51] Annealing led to the appearance of extra peaks at 127, 172 and 249 cm^{-1} with variation in intensity. The peak at 127 cm^{-1} is related to the γ-In_2Se_3 phase.[51] The latter two Raman peaks were attributed to the Te–Te[52] bond vibration and Se_n rings.[50,53] The intensity increase in the Raman peaks and low shift towards higher wavenumbers with annealing might be due to annealing-induced structural changes inside the matrix.

3.2. Morphology study using FESEM and EDX

For imaging the microstructure and morphology study of any material, FESEM is one of the most important tools. The morphological structure of the $In_{10}Se_{70}Te_{20}$ (as-prepared and annealed) thin films was analysed by FESEM images, as shown in Fig. 2. The morphological images at a scale of 200 nm illustrate the uniformity of the films. The annealing-induced morphological changes were clearly observed in the granular structure of the annealed films. The particle size was calculated using ImageJ software (version-Java 1.8.0_172), with statistical analysis, as presented in Fig. 3. With an increased annealing temperature, the average particle size increased, as demonstrated in Fig. 3.

Elemental analysis was performed using EDX, which showed the presence of In, Te, and Se components (Fig. 4) in the annealed and as-prepared films. The distinct peaks refer to the relevant components, and the composition of the various samples is closely the same within a 2% error of the estimated one. The uniform distribution of constituent elements through elemental mapping obtained from EDX for the as-deposited $In_{10}Se_{70}Te_{20}$ film is shown in Fig. 5, and the 250 °C annealed film is shown in ESI Fig. S1.†

3.3. Optical property study

3.3.1. Transmittance, optical density, extinction coefficient and skin depth. The variation in transmittance with wavelength for $In_{10}Se_{70}Te_{20}$ (both in as-prepared and annealed) thin films is presented in Fig. 6a, which infers an increase in transmission power upon annealing. The transmittance value increased from 35% (as-prepared) to 76% for the 250 °C annealed film at a 1900 nm wavelength. This increase in the transmittance value is due to the increase in crystallinity with annealing.[54] The enhanced transmission is also owing to the decrease in surface scattering with annealing.[55,56] The transparency is found to be more in the infrared region, which allows such films for potential use in infrared systems, such as fiber optics.[57] The observed interference pattern in the film is due to the interference between the substrate and film surface.

The optical absorbance provides valuable information related to the bandgap and band structure of both crystalline and amorphous materials. There is a shift in the absorption edge to the lower wavelength side, which is due to the thermal bleaching effect, thus inferring an increase in bandgap energy

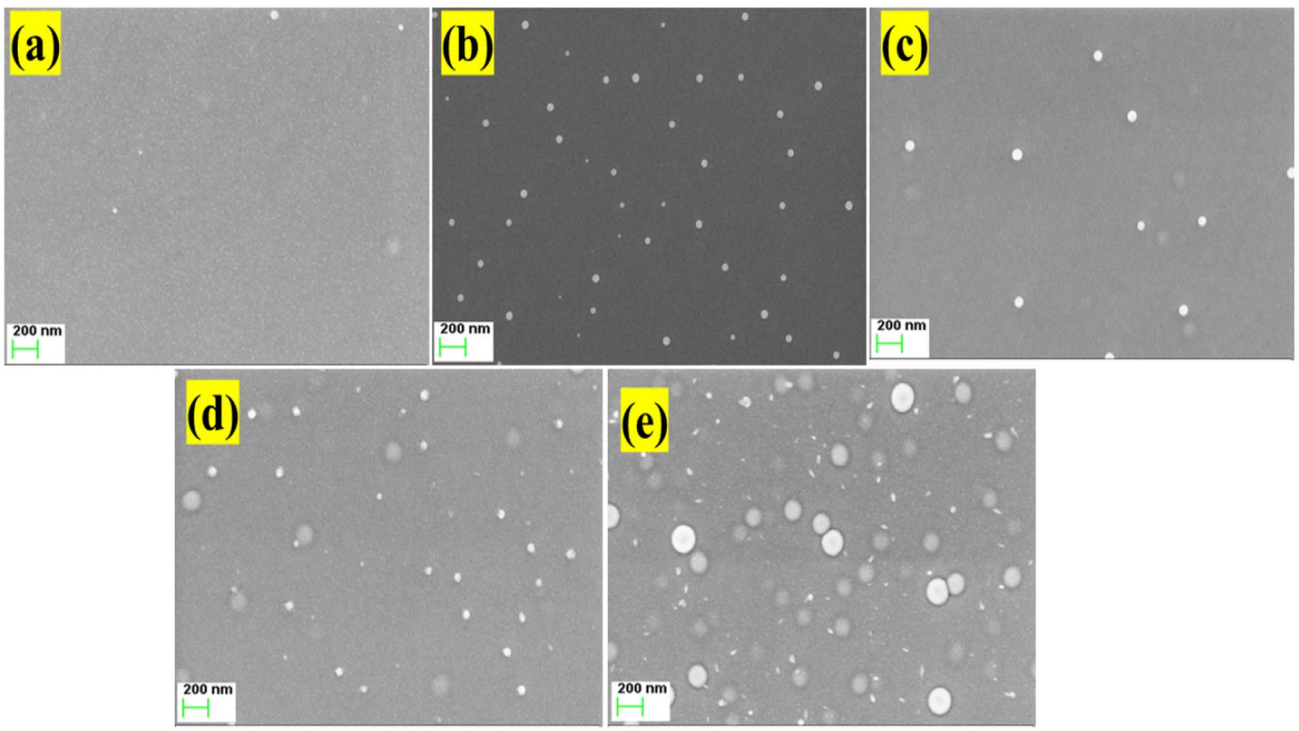

Fig. 2 FESEM images for surface morphological analysis of $In_{10}Se_{70}Te_{20}$ thin films.

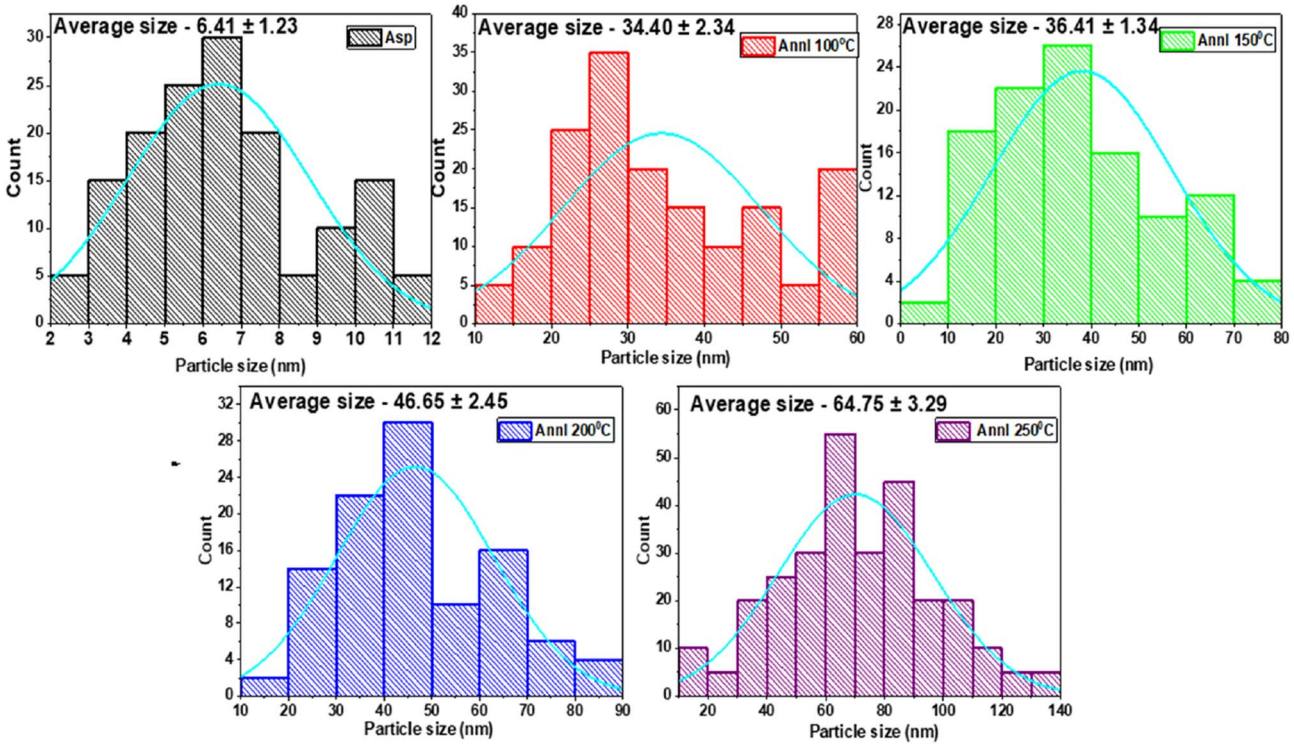

Fig. 3 Particle size distribution of the $In_{10}Se_{70}Te_{20}$ thin films.

with annealing.[58] The optical absorption edge appears because of the electronic transition in the semiconductor.[58,59] Here, the absorption edge region lies in the range of 750–1200 nm, and the coefficient (α) was determined from the absorbance value using the following equation:

$$\alpha = \frac{\text{absorbance}}{\text{thickness}} = \frac{A}{t}, \quad (4)$$

where 'A' and 't' are the absorbance and film thickness, respectively. The absorption coefficient measures the rate of reduction in electromagnetic radiation intensity while

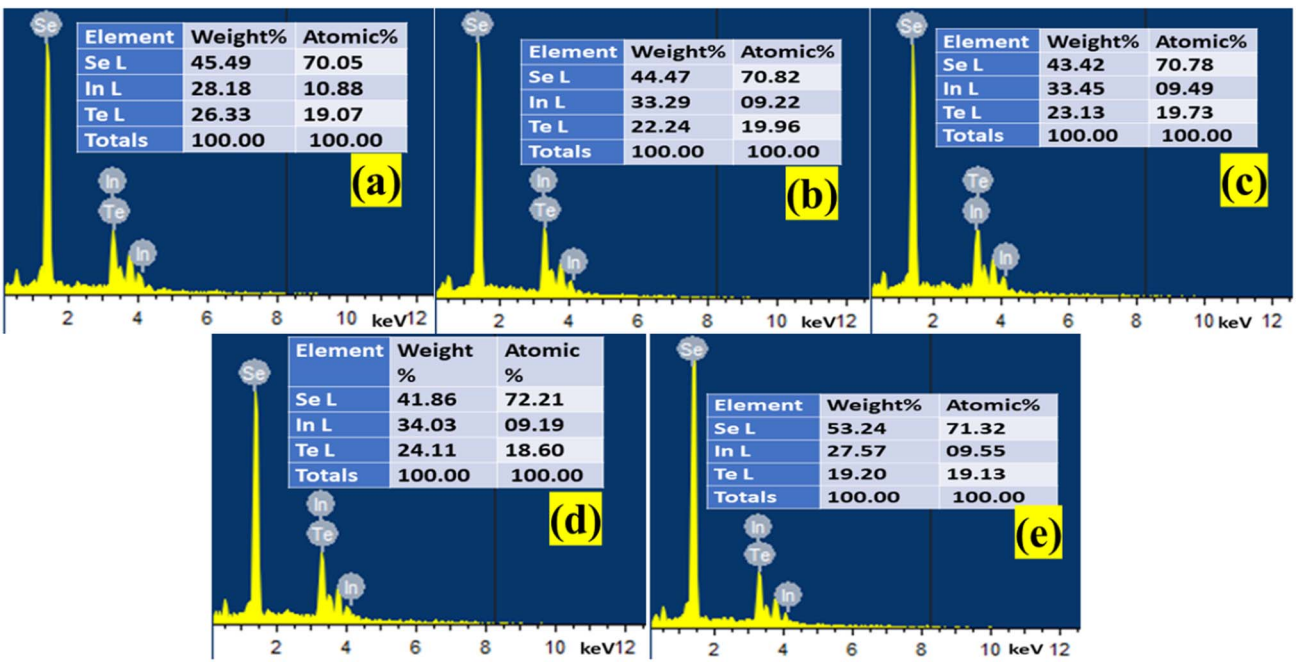

Fig. 4 EDX spectra for compositional analysis of $In_{10}Se_{70}Te_{20}$ thin films.

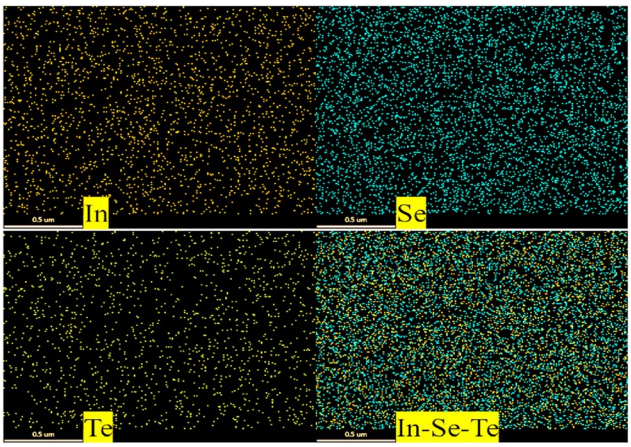

Fig. 5 EDX mapping of the elements in the as-prepared $In_{10}Se_{70}Te_{20}$ film.

penetrating through a material medium. The greater the absorption of light by the material, the higher the absorption coefficient.[59] The change in 'α' with wavelength under various annealing conditions is shown in Fig. S2.† The 'α' values are in the order of 10^4 cm^{-1}, which decreased with annealing and increased with photon energy. The presence of such absorption edges makes them a potential candidate for optical filter materials.[60]

Thermal annealing at and above T_g minimizes the structural imperfections, resulting in few available states for photon absorption within the band gap. The local structure in the film changes because of the bond breaking and rearrangements due to annealing. This results in a shift in the absorption edge and substantial reconfiguration at the atomic and molecular levels, ultimately changing the optical parameters of the film.[61]

The extinction coefficient (k) represents the polarization ability of the material, which is dependent on 'α' using the following formula:[56] $k = (\alpha\lambda/4\pi)$. The 'k' infers the interaction between the electric field of the incident waves and the film. The 'k' value decreased with wavelength, as shown in Fig. 6b for the annealed and as-deposited one. This behaviour is owing to the decrease in 'α' with an increase in 'λ'. The heat treatment annealed out the unsaturated defects and produced a large number of saturated bonds after annealing. The density of the localized state change because annealing modifies the 'k' value.[62] The as-prepared $In_{10}Se_{70}Te_{20}$ sample showed crystallinity with the appearance of In_2Te_3 and In_4Se_3 phases. The increase in the annealing temperature led to an increase in crystallinity. This might be due to the annealing process that provides sufficient energy to the atoms, enabling them to

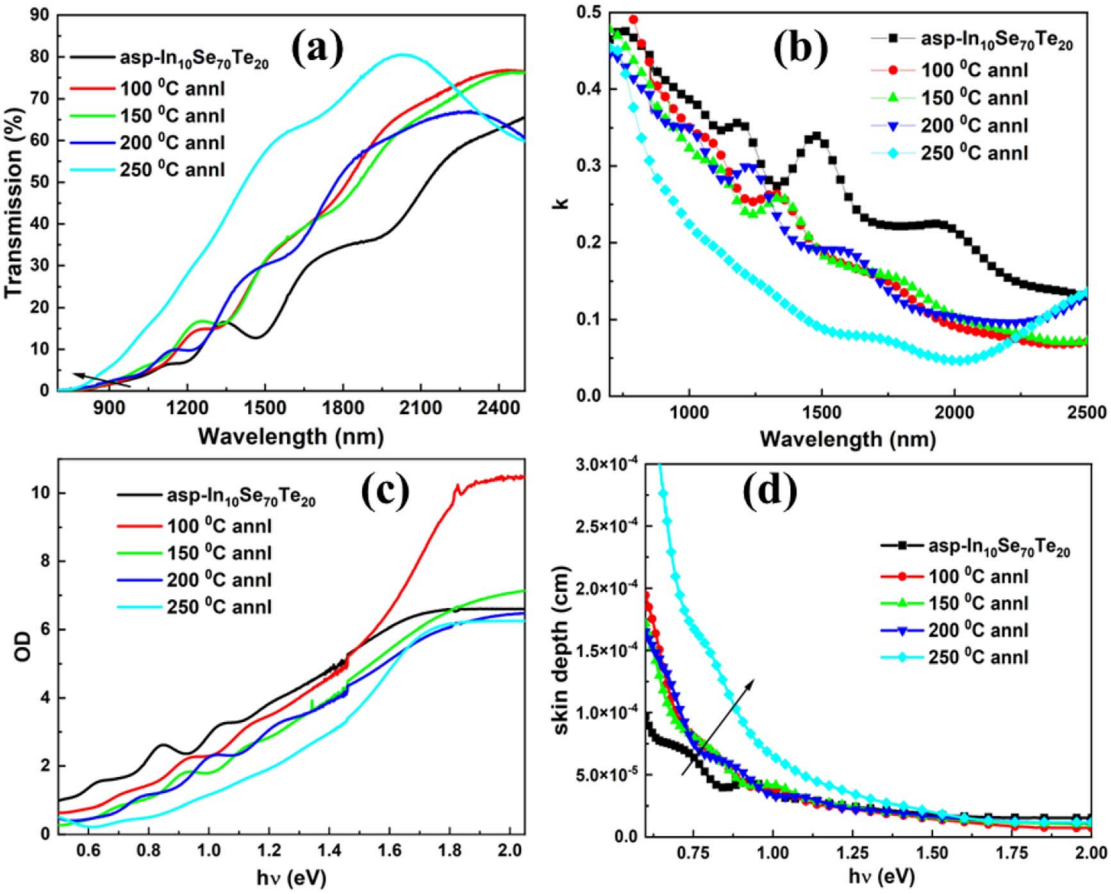

Fig. 6 Change in (a) transmittance, (b) extinction coefficient with wavelength, (c) optical density and (d) skin depth with energy of $In_{10}Se_{70}Te_{20}$ thin films.

migrate from their relative equilibrium position. Consequently, grain growth increases, and lattice dislocation decreases. This causes an increase in lattice perfection and lattice growth.[63,64] This causes changes in the optical properties by improving the transmittance and shifting the absorption edges. The blue shifting in the absorption edge reduced the absorption coefficient, representing light absorption through the material medium. The extinction coefficient, refractive index, and nonlinear parameters are all related to the absorption coefficient. Therefore, these parameters showed a reducing pattern with annealing temperature.

The absorption capability of the film is also represented by another optical quantity so called optical density (OD). It signifies the degree to which a refractive medium retards transmitted light rays. Fig. 6c depicts the change in OD ($= \alpha \times t$, where 't' is the film thickness and 'α' is the absorption coefficient), which decreased with an increase in annealing temperature. In thin films, OD is due to the refraction and scattering of light, measuring the velocity of light in the material.[65] The absorbance is very low (below 2%) at a lower $h\nu$, which leads to an enhancement in the transmittance of electromagnetic waves in a low absorbance regime. This behavior is responsible for the high IR transmission in In–Se–Te chalcogenide thin films. The decrease in OD value accounts for the increase in the velocity of light inside the material with annealing. The material concentration decreased, resulting in an increase in optical transparency as obtained in the transmission spectra.

The penetration depth, so-called skin depth (δ), is measured as the length scale at which the absorbance of incident photon becomes $1/e$ of its value inside the film surface. The value of δ is calculated from $1/\alpha$.[65] It is clear from Fig. 6d that the skin depth increased with annealing at lower photon energy but decreased because of a lower value at high photon energy. The cut off energy (E_{cutoff}) is defined as the photon energy at which δ is having nearly zero value for all the investigated samples. The E_{cutoff} value is 1.75 eV for the investigated films. The cut off wavelength (λ_{cutoff}) is the wavelength corresponding to the cut off energy, and its value is ~708 nm for the investigated films.

3.3.2. Optical bandgap, Tauc parameter, and Urbach energy. The optical absorption phenomena at the fundamental edge are discussed using the concept of a band-to-band transition. Absorption occurs by absorbing photons with energy equal to or more than the band gap. The electronic transition probability across the forbidden gap measures the absorption coefficient, which is the number of absorbed photons per incident photon. The optical bandgap of the material can be determined by the absorption coefficient. Using the absorption coefficient, photon energies are approximately equal to the bandgap energies of chalcogenides. In the first region, there is a weak absorption region ($\alpha < 1$ cm^{-1}), where the absorption depends on the synthesis, purity of material and temperature history. The second region ($10 < \alpha < 10^4$ cm^{-1}) corresponds to the Urbach region, where the absorption occurs in between localized and extended states. In the third region, a higher absorption coefficient ($\alpha > 10^4$ cm^{-1}) was observed in the Tauc region.[59] The optical bandgap due to structural randomness was calculated using the following Tauc equation:[66]

$$\alpha h\nu = C(h\nu - E_g)^p, \quad (5)$$

where 'C' and 'p' are the Tauc parameter and exponent, respectively. The term 'p' refers to the transition-mode power factor, which decides the type and nature of electronic transition in the gap. It has different values, such as $p = 2$ (indirect allowed), 1/2 (direct allowed), 3 (indirect forbidden) and 3/2 (direct forbidden) transitions.[56,61] The investigated thin film absorption data fits for $p = 2$, suggesting the indirect allowed transition type. Fig. 7a–e shows the plot of $(\alpha h\nu)^{1/2}$ *vs.* $h\nu$ and depicts the indirect allowed transition. The straight-line fitting of the linear portion, which cuts the X-axis, gives the E_g value (Table 2).

The E_g value of the as-prepared $In_{10}Se_{70}Te_{20}$ film was 0.418 eV, which increased to 0.645 eV upon annealing at 250 °C temperature. The E_g values for the other films are shown in Table 2, which shows an increasing trend with annealing. The enhancement in E_g value with annealing is explained by the Mott and Davis theory.[67] A large number of saturated bonds are formed by annealing unsaturated bonds at the above crystallization temperature. Such a decrease in unsaturated defects causes a reduction in the density of localized states in the gap and ultimately enhances the band gap.[68] In other way, according to the chemical bond approach, the formation of greater bond energy-based bonds such as In–Se (53.64 kcal mol^{-1}), Se–Te (44.18 kcal mol^{-1}) and In–Te (33.05 kcal mol^{-1}) occurs at first, followed by low energy-based bonds Te–Te (33 kcal mol^{-1}) and Se–Se (44 kcal mol^{-1}).[49,69,70] The local structure in the film changed by bond breaking and bond arrangement due to annealing the thin films. Therefore, the low-energy bonds along with some dangling bonds were annealed with the formation of stronger bonds In–Se and In–Te bonds. This behaviour was also satisfied by the XRD and Raman studies. The formation of stronger saturated bonds in place of dangling bonds results in the reduction of the density of defect states over the gap region and enhances the band energy. Such effects bring changes in the absorption edge shift and reorganization at the atomic and molecular levels, modifying the optical parameters. According to Surbhi *et al.*, the temperature dependency of the bandgap in semiconductors is often related to an increase in interatomic separation as the magnitude of atomic vibration rises with an increase in thermal energy, which leads to an increase in the electron–lattices interactions.[71]

The parameter C is an indicator of the degree of structural disorder for semiconducting materials. The value of C was evaluated from the slope of the fitting, as shown in Fig. 7a–e. The low value of C depicts more structural disorders.[72] Thus, the higher C value (see Table 2) for the annealed films than for the as-deposited ones infers a reduction in structural disorder with annealing. Liu and colleagues studied the annealing-induced absorption and photoluminescence (PL) study of PbS QDs, which showed that an increase in annealing duration led to improved absorption and PL response.[73] However, in our case, the annealing duration was kept at a fixed duration, *i.e.* 1.5 h, with varying temperatures in the range of 100–250 °C. Such variation in annealing temperature led to a reduction in the 'α' of the material. Similarly, Gami *et al.* synthesized (6,6)-phenyl

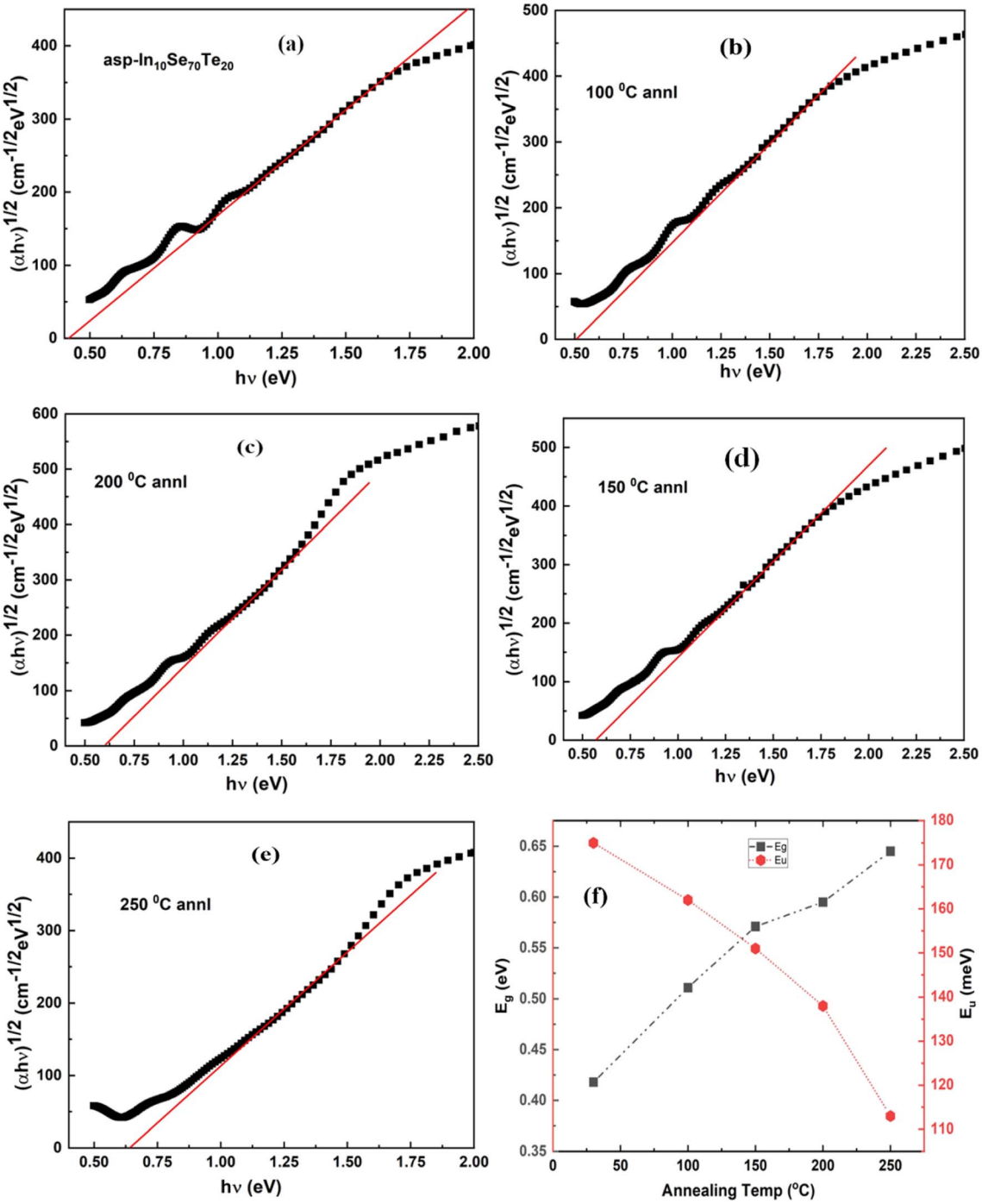

Fig. 7 (a–e) Optical bandgap of as-deposited and annealed $In_{10}Se_{70}Te_{20}$ films and (f) variation of E_g, which is the Urbach energy with annealing temperatures.

C61 butyric acid methyl ester (PCBM)/Zinc(II) octaethylporphyrin (ZnOEP) thin film using the spin coating method. By varying the PCBM/ZnOEP thin film layer thickness, the E_g value was reduced, which is due to the creation of defects by the PCBM film. Thus, the Tauc parameter (B) was reduced, indicating that the PCBM content influenced the disorder of ZnOEP/PCBM.[74] Surbhi *et al.* investigated the optical response of $Te_{1-x}(GeSe_{0.5})Sc_x$ ($x = 0$, 0.05, 0.1, and 0.15) (TGSS) thin films, which showed enhancement in the E_g with Sc doping. Here, the Tauc parameter (A) showed a reduction pattern as Sc increases, signifying the influence of doping in the TGSS film. This competition could be utilized for optical storage applications. The observed E_g range in TGSS is 1.18 eV–1.27 eV, which is slightly close to the currently observed values. Therefore, this In–Se–Te film might also be a possible application for optical storage applications.[75] Furthermore, Dongol *et al.* investigated

Table 2 Variation in optical parameters of $In_{10}Se_{70}Te_{20}$ thin films

Optical parameter	As-prepared	100 °C	150 °C	200 °C	250 °C
E_g (eV)	0.418 ± 0.03	0.511 ± 0.01	0.571 ± 0.01	0.595 ± 0.04	0.645 ± 0.02
$C^{1/2}$ ($cm^{-1/2}$ $eV^{-1/2}$)	208	229	241	256	301
E_U (meV)	175	162	151	138	113
$\sigma \times 10^{-2}$ (steepness parameter)	14.8	15.98	17.15	18.76	22.92
S_{e-p}	4.504	4.172	3.887	3.554	2.909
E_d (eV)	0.1192	0.0804	0.0420	0.0371	0.0311
E_o (eV)	1.438	1.440	1.467	1.476	1.511
$f = E_oE_d$	0.1714	0.1157	0.0616	0.0547	0.0469
M_{-1}	0.0828	0.0558	0.0286	0.0251	0.0205
M_{-3}	0.0400	0.0269	0.0132	0.0115	0.00897
n_0	1.041	1.027	1.0142	1.0126	1.010
ε_∞	1.0836	1.0547	1.0286	1.0253	1.0201
λ_o (nm)	734.01	721.05	701.81	685.34	667.25
S_0 ($nm^2 \times 10^{-8}$)	12	6.6	4.3	3.7	3.5
ε_L	7.669	6.582	5.208	3.608	2.255
N/m^* (m^{-3} kg^{-1}) $\times 10^{39}$	9.2	7.96	6.44	4.21	3.01
Plasma frequency ω^2 ($\times 10^{11}$)	8.67	8.74	8.94	9.13	9.65
η_{opt}	2.225	2.233	2.240	2.241	2.242
χ^1 (esu) $\times 10^{-3}$	6.65	4.35	2.27	2.01	1.60
χ^3 ($h\nu \rightarrow 0$) $\times 10^{-22}$ (esu)	3324	608.7	45.13	27.74	11.14
n_2^T (esu)	1.2×10^{-17}	2.23×10^{-18}	1.67×10^{-19}	1.03×10^{-19}	4.15×10^{-20}
n_2^F (esu)	2.38×10^{-20}	1.05×10^{-20}	2.77×10^{-21}	2.15×10^{-21}	1.36×10^{-21}

the annealing-induced optical properties of $Ge_{20}Se_{65}S_{15}$ thin films, which showed a reduction pattern in the absorption coefficient with an increment in E_g from 2.07 eV to 2.13 eV. Such behavior is due to the creation of more numbers of saturated bonds in place of unsaturated bonds. Here, the Tauc parameter (B) value showed an increased trend, indicating a lower structural disorder with annealing. Such annealing-induced optical tuning in the $Ge_{20}Se_{65}S_{15}$ thin film could be effectively used in photonic device fabrication.[76]

The presence of impurities and defects in the film results in a weak absorption region in which 'α' shows exponential variation with $h\nu$. Such an absorption edge indicates the existence of a localized state in the gap. The band tailing is due to random fluctuations in internal fields, causing structural disorders.[77] The energy corresponding to this region is called the Urbach energy (E_U), which is evaluated from Urbach's relation:[78]

$$\alpha(h\nu) = \alpha_0 e^{\frac{h\nu}{E_U}}, \quad (6)$$

where α_0 is the value of the absorption coefficient at the bandgap point. E_U value (given in Table 2) is determined as the reciprocal of the slope of the straight-line fitting between $\ln(\alpha/\alpha_0)$ *versus* $h\nu$ graph. E_U represents the width band tails in localized states that indicate the amount of disorder in the semiconductor. According to Surbhi *et al.*, the change in the E_U is related to the density of defect states in the regime of the bandgap.[75] The decrease in E_U value from 175 meV (as-prepared) to 113 meV for the 250 °C annealed film indicates a reduction in the density of defect states over the band gap. Thus, annealing results in a decrease in disorder and defects inside the matrix. The decrease in E_U value and increase in E_g value under different annealing conditions are shown in Fig. 7f.

The broadening in the absorption edge is represented by the steepness parameter (σ), which is because of excitation due to electron–phonon or excitation–phonon interaction. This parameter is evaluated by the relation[77] $\sigma = KT/E_U$, where T is temperature, E_U is the Urbach energy, and K is the Boltzmann constant. The obtained σ values are presented in Table 2 and shown in Fig. 8a, depicting an increase in σ with annealing. This confirms the increase in the optical bandgap due to the broadening of the gap.

The interaction strength between electrons and phonons is represented by S_{e-p}. The knowledge of lattice expansion and the increase in lattice constants is obtained from S_{e-p}. The increase in S_{e-p} value infers the increase in lattice dimensions and *vice versa*. The S_{e-p} value is calculated by $S_{e-p} = 2/3\sigma$,[77] as demonstrated in Table 2. Considering that increasing the lattice dimensions leads to decreasing the band-gap energy, the decrease in the S_{e-p} value with annealing results in an increase in the E_g value, as shown in Fig. 8b.

The decreased S_{e-p} values are in good correlation with the increased E_g value because of their inverse relationship with each other. Because of the peculiar optical properties of In–Se–Te thin films, they are considered for many optoelectronic applications and devices, such as photonic circuits, photovoltaics, signal preparing, solar cells, optical fibers, photolithography, and optical recorders.

3.3.3. Refractive index and dispersion parameters. Refractive index (n) is an indicator of light dispersion and is useful for non-linear phenomena. This is one of the important optical parameters required for strong optical field confinement, which allows for small waveguide bend radii and enhanced optical intensities.[59] It depicts useful information related to both the linear and non-linear parameters of the sample. The value of 'n'

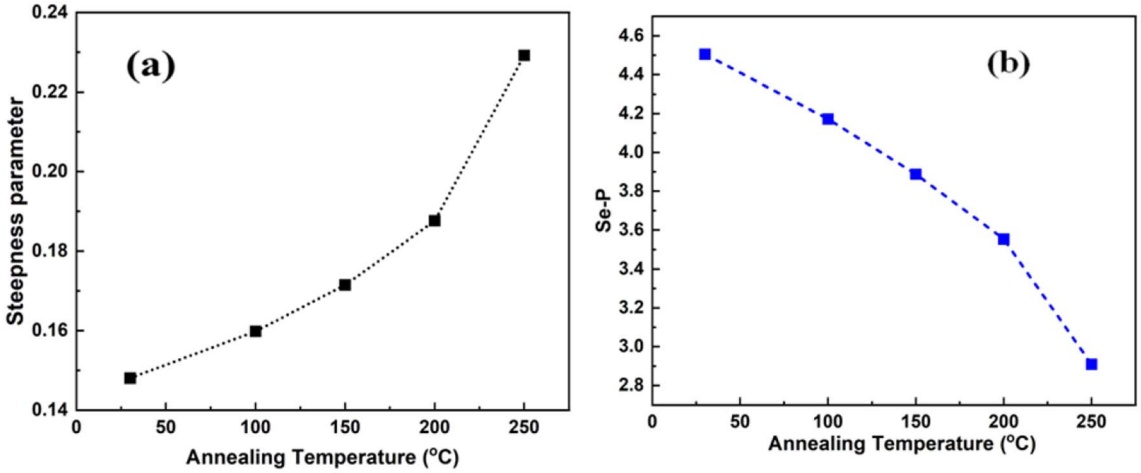

Fig. 8 (a) Increase in steepness parameter and (b) decrease in S_{e-p} value at different annealing temperatures.

was calculated from the transmission data using the following formula:[79]

$$n = \left(\frac{1}{T-1}\right)^{1/2} + \frac{1}{T}. \quad (7)$$

Fig. 9a shows the refractive index change at different 'λ', showing the normal dispersion behaviour of the film. The value of 'n' decreased with annealing temperature with a simultaneous increase in E_g. In the lower wavelength regime, the 'n' value is large, whereas in the upper wavelength region, it

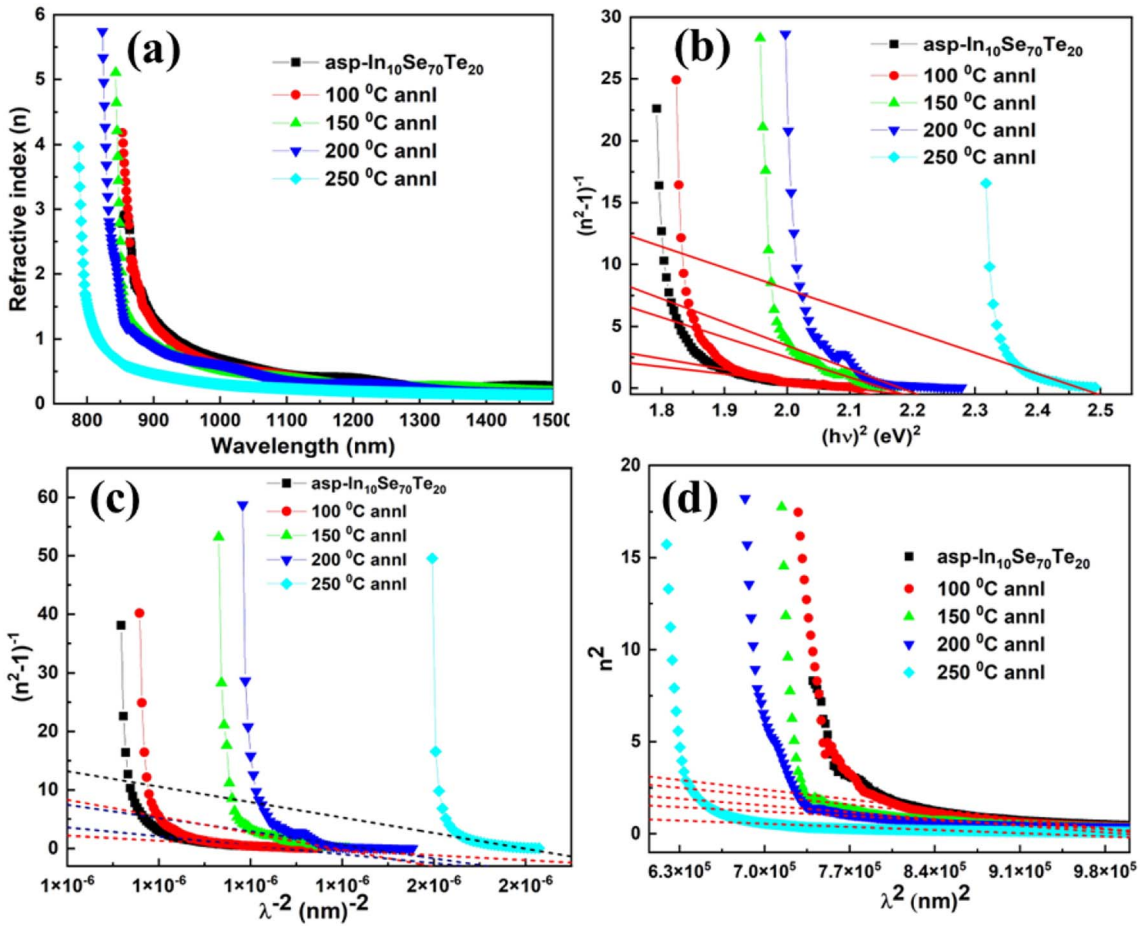

Fig. 9 (a) Variation in 'n', (b) $(n^2-1)^{-1}$ *vs.* $(h\nu)^2$ graph, (c) $(n^2-1)^{-1}$ *vs.* $(\lambda)^{-2}$ graph and (d) n^2 *vs.* λ^2 graph of $In_{10}Se_{70}Te_{20}$ thin films.

decreases to a saturated value. The absorption capability is more at higher frequencies for which the speed of light decreases and the *n*-value increases. The optical field confinement is more at a high value of '*n*', which maintains the small waveguides to bend inside the fibre. Thus, the optical intensities increase for which the material becomes more efficient and useful for non-linear interactions.[80]

The variation in refractive index is associated with the change in bandgap by Moss rule, *i.e.*, $E_g n^4 \sim$ constant.[81] The valence band is formed by lone pair orbitals, and the antibonding orbital forms the conduction band. With the increase in annealing temperature, there is excitation of bonding states and lone-pair electrons to the antibonding states. The vacancy created by this process is filled by the outer electrons and leads to the increase in lone-pair, holes and bonding orbitals, resulting in the formation of vacancy.[61] Such bond rearrangement favors the local structure to change and reduces '*n*' and '*k*' values at higher annealing temperatures.

The dispersion parameters play an important role in designing various spectral dispersion and optical communication devices. Single oscillator (E_o) and dispersion (E_d) energy are two essential parameters for optical devices. The E_d is independent of E_o because E_d depends on the dielectric loss, whereas E_o does not depend on the dielectric loss. The Wemple-DiDomenico model is related to E_o, E_d and hν. E_o is regarded as the average energy gap that gives information on the band structure, while E_d carries the average inter band optical transition strength, in which the E_d value decreased because of the annealed films. It is related to structural parameter change in the material, such as coordination number (N_c), ionicity (β = 0.37 eV), the effective number of valence electrons per anion (N_e) and anion valency (Z_a) of the material by $E_d = \beta N_c Z_a N_e$ (eV).[76] The structural disorder and physical properties of the material are associated with 'E_d'. The decreased value of E_d for the present case with annealing infers less structural disorder.

The single effective oscillator model provides an in-depth physical interpretation of the measured parameters. The model is presented by the following equation:[54]

$$\left(n^2-1\right)^{-1} = \frac{{E_o}^2-(h\theta)^2}{E_o E_d} = \frac{E_o}{E_d} - \frac{(h\theta)^2}{E_o E_d}. \quad (8)$$

The calculations of E_o and E_d were performed from the graph between $(n^2-1)^{-1}$ *vs.* $(h\nu)^2$, as depicted in Fig. 9b. The E_o and E_d values are evaluated from the slope and intercept of the fitting, as depicted in Table 2. It is noticed that E_o increased while E_d decreased with an increase in the annealing of $In_{10}Se_{70}Te_{20}$ film. The lattice dielectric constant (ε_∞) and static refractive index (n_0) were calculated using the following formula:[45,54]

$$\varepsilon_\infty = 1 + \frac{E_d}{E_o}, \quad n_0 = \sqrt{1+\frac{E_d}{E_o}}. \quad (9)$$

The quantity $f = E_o E_d$ refers to the oscillator strength of the material, which decreased with an increase in annealing, as shown in Table 2. It is found that ε_∞ decreased with annealing of $In_{10}Se_{70}Te_{20}$ film.

The two moments of spectra first-order (M_{-1}) and third-order (M_{-3}) were evaluated by E_o and E_d using the following equations:[45,52]

$$M_{-1} = E_d/E_o \text{ and } M_{-3} = M_{-1}/{E_o}^2. \quad (10)$$

The values of both M_{-1} and M_{-3} decreased with the annealing of $In_{10}Se_{70}Te_{20}$ films, as shown in Table 2.

At the lower frequency region, the '*n*' value satisfies the following Sellmeier's dispersion model:[45,76]

$$\left(n^2-1\right)^{-1} = \frac{1}{s_0{\lambda_0}^2} - \frac{1}{s_0\lambda^2}. \quad (11)$$

The straight-line fitting of $(n^2-1)^{-1}$ *vs.* $(\lambda)^{-2}$ (Fig. 9c) evaluates the value of 's_0' (strength of the oscillator) and λ_0 (oscillator wavelength). The decreases in λ_0 and s_0 values with annealing of $In_{10}Se_{70}Te_{20}$ films are shown in Table 2 λ_o is inversely proportional to E_o, and E_o is directly proportional to E_g, which leads to $\lambda_o \propto 1/E_g$. Consequently, λ_o decreased due to the improvement in the crystallinity and change in the surface morphology of the films.[82]

3.3.4. High-frequency dielectric constant (ε_L) and dielectric parameters and plasma frequency. The 'ε_L' and carrier concentration per effective mass (N/m^*) were calculated from the variation of '*n*' with 'λ' using the following equation:[54,57]

$$n^2 = \varepsilon_L - \left(\frac{e^2}{4\pi^2 c^2 \varepsilon_0}\right)\left(\frac{N}{m^*}\right)\lambda^2. \quad (12)$$

The plot between λ^2 and n^2, as presented in Fig. 9d, evaluates the value of N/m^* and ε_L from its intercept and slope. The N/m^* decreased from 9.2×10^{39} m^{-3} kg^{-1} of the as-prepared film to 3.01×10^{39} m^{-3} kg^{-1} for the 250 °C annealed film. This shows the microstructural changes in the film, as shown in Fig. 2. The change in the orientation of dipoles present in chalcogenide films led to variations in ε_L. Although both the values of ε_L and ε_∞ are very close to each other, the decrease in both values upon annealing films is due to the increase in polarization.[83] The lower value of ε_∞ compared to ε_L is due to the contribution of free charge carriers to the polarization process, which has also been observed in other studies.[84]

The value of the plasma frequency (ω_p) is evaluated using the following Drude relation:[85]

$$\frac{N}{m^*} = \left(\frac{\varepsilon_0 \varepsilon_\infty}{e^2}\right){\omega_p}^2$$

Or

$$\omega_p = \left[\left(\frac{e^2}{\varepsilon_0 \varepsilon_\infty}\right)\frac{N}{m^*}\right]^{1/2}. \quad (13)$$

The calculated ω_p values for the films are listed in Table 2. At the plasma frequency, the oscillation of free charge carriers achieves its peak. There is no other resonance except the plasma frequency, and the radiation of the material travels in the

dielectric material and is reflected in the lower frequency. Here, ω_p increased with thermal annealing for the studied films.

The dielectric constant is the built-in property of a semiconductor that defies the behavior under an applied electric field. The complex dielectric constant has both real (ε_r) and imaginary (ε_i) parts, $\varepsilon^* = \varepsilon_r + i\varepsilon_i$). Additionally, in terms of 'n' and 'k', it is expressed as $\varepsilon^* = (n + ik)^2$. The dielectric loss tangent (tan δ) was evaluated from ε_r and ε_i. The ε_r gives an idea of the de-acceleration of incident energy during propagation inside the films. The 'ε_i' accounts for the loss of energy and is called the damping factor. This parameter measures the energy loss and dissipation inside the material during the passing of light waves inside it.[85] The ratio $\varepsilon_{i/}\varepsilon_r$ evaluates the loss factor, and these parameters are evaluated using the following formulas:[85]

$$\varepsilon_i = 2nk \text{ and } \varepsilon_r = n^2 - k^2. \quad (14)$$

Fig. 10a and b show the variation in ε_r and ε_i with $h\nu$, and both parameters decreased with the annealing of $In_{10}Se_{70}Te_{20}$ films. The comparatively high value of ε_r than ε_i is due to the changes in 'n' and 'k'. The figures clearly show that the 'ε_1' is seven times greater than the 'ε_2'. This is because $n \gg k$ in the '1' case, whereas in the 'ε_2' case, the low 'k' value reduced the imaginary part to less than 5.

The dielectric loss factor measures the energy absorbed by the material when the electromagnetic wave passes inside it. This parameter also depicts the phase difference in the loss of energy at a fixed frequency (Fig. 10c). The value of 'tan δ' is more for the annealed film at high photon energy. The nature of change in tan(δ) is similar to the 'k' value, which infers the dominating nature of dielectric loss in this electromagnetic regime over optical absorption. The quality of oscillation so-called quality factor (Q)[85] is the inverse of tan(δ), *i.e.* $Q = \varepsilon_{r/}\varepsilon_i$. The Q factor is found to decrease with the annealing of $In_{10}Se_{70}Te_{20}$ films, as shown in Fig. 10d.

The moving electron losses energy while moving within the sample during its motion owing to plasma oscillations, which are excited in a sea of conduction band electrons. The degree of such loss of energy is associated with the optical features of any material. The energy loss functions are essential quantities for shedding light on damping on the surface or within the films. The average free path of the inelastic electron during its travel inside the sample is measured by such an energy loss function. Thus, it is essential to calculate the volume energy losses (VELF) and surface energy loss function (SELF). The VELF and SELF are evaluated using ε_r and ε_i as follows:[82,85]

$$\text{VELF} = \frac{\varepsilon_i}{{\varepsilon_r}^2 + {\varepsilon_i}^2}, \quad \text{SELF} = \frac{\varepsilon_i}{(\varepsilon_r + 1)^2 + {\varepsilon_i}^2}. \quad (15)$$

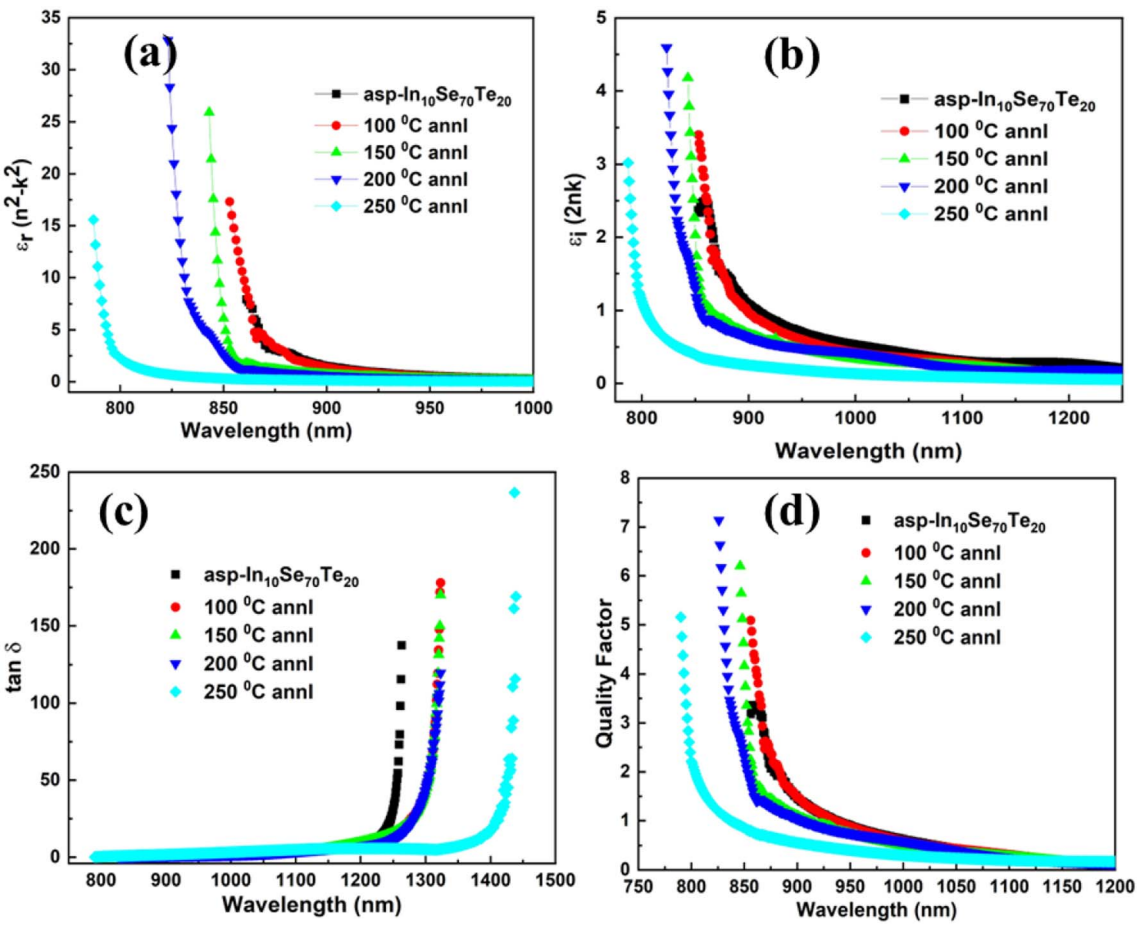

Fig. 10 (a) ε_r *vs.* $h\nu$, (b) ε_i *vs.* $h\nu$, (c) tan(δ) *vs.* $h\nu$ plot and (d) quality factor *vs.* $h\nu$ plot for as-prepared and annealed $In_{10}Se_{70}Te_{20}$ thin films.

Both VELF and SELF define the absorption of energy of a material that signifies losses and is also related to a single transition of electrons in the semiconductor. The variation in VELF and SELF with λ is given in Fig. 11a and b, from which it is evident that VELF increased with annealing whereas SELF decreased with annealing.

3.3.5. Optical conductivity and optical electronegativity (η_{opt}). The optical response of the sample is measured from its optical conductivity (σ) value. The amount of light propagation through the medium in a certain wavelength regime is obtained from 'σ'. The study of the complex 'σ' of films is essential owing to their functional applications. The 'σ' value is dependent on ε_r and ε_i. The 'σ' value infers the electronic state density within the bandgap of the material.[86] The complex $\sigma^*_{opt} = \sigma_r(\omega) + i\sigma_i(\omega)$ has both real and imaginary components. The $\sigma_i(\omega) = \omega\varepsilon_o\varepsilon_r$ and $\sigma_r(\omega) = \omega\varepsilon_o\varepsilon_i$, where ω is the angular frequency. Fig. 11c and d show the variation in real and imaginary optical conductivities with photon energy. There is a rapid increase in both $\sigma_i(\omega)$ and $\sigma_r(\omega)$ as energy increases. This increment in both optical conductivities is explained by an increment in the absorption coefficient at a higher energy or lower wavelength. This behaviour has also been observed in other studies.[75] Both values decreased upon annealing the $In_{10}Se_{70}Te_{20}$ films.

The degree of polarization so called electrical susceptibility (χ_c) is denoted as follows:[87]

$$\chi_c = \frac{1}{4\pi}\left[n^2 - k^2 - n_0{}^2\right] = \frac{1}{4\pi}\left[\varepsilon_r - n_0{}^2\right]. \quad (16)$$

The value of χ_c is shown in Fig. S3,† which indicates the decreasing trend with annealing and a higher value at a high value of $h\nu$.

The presence of lone pairs is linked with polarization by optical electronegativity (η_{opt}). The value of η_{opt} in terms of n_o is given as follows:[86,87] $\eta_{opt} = \left(\frac{C}{n_0}\right)^{1/4}$, where $C = 25.54$. The evaluated η_{opt} values increased with annealing for $In_{10}Se_{70}Te_{20}$ films, as shown in Table 2. Because η_{opt} is related to the refractive index, the optical electronegativity also affects the non-linear parameters.

3.3.6. Non-linear optical properties. The non-linearity in the films originates when the high-intensity electromagnetic wave incident on it and is governed by the Kerr effect: $\Delta n_o = n_2 \times I$, where I is the optical intensity and n_2 is the non-linear refractive index. The origin of non-linearity is due to the interactions of electronic polarization, which affects the bond length of the material.[45] The idea of non-linear optical entities of a material determines the propagation characteristics of light through it. The polarization P is expressed as follows:[38]

$$P(t) = \varepsilon_0[\chi^1 E(t) + \chi^2 E(t)^2 + \chi^3 E(t)^3 + \ldots], \quad (17a)$$

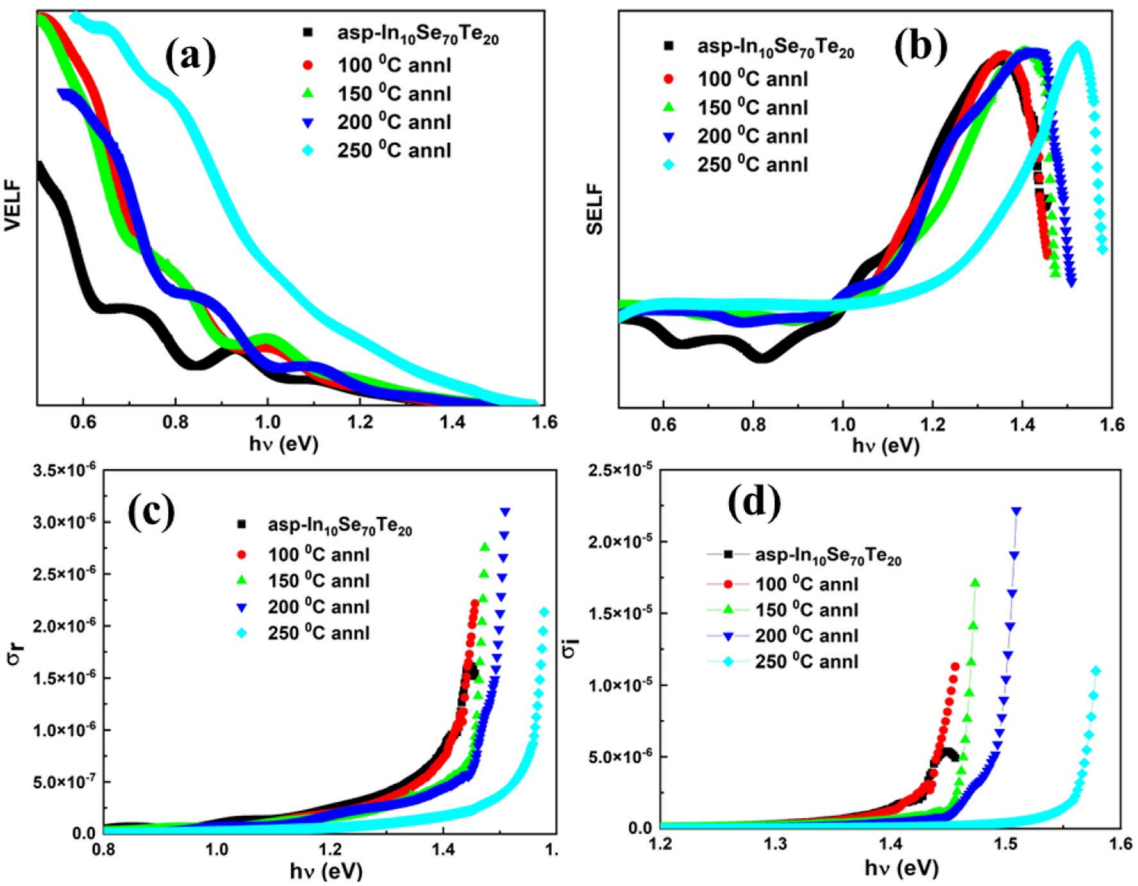

Fig. 11 (a) Change in VELF, (b) SELF with $h\nu$, (c) variation in σ_r and (d) σ_r with $h\nu$ for $In_{10}Se_{70}Te_{20}$ films.

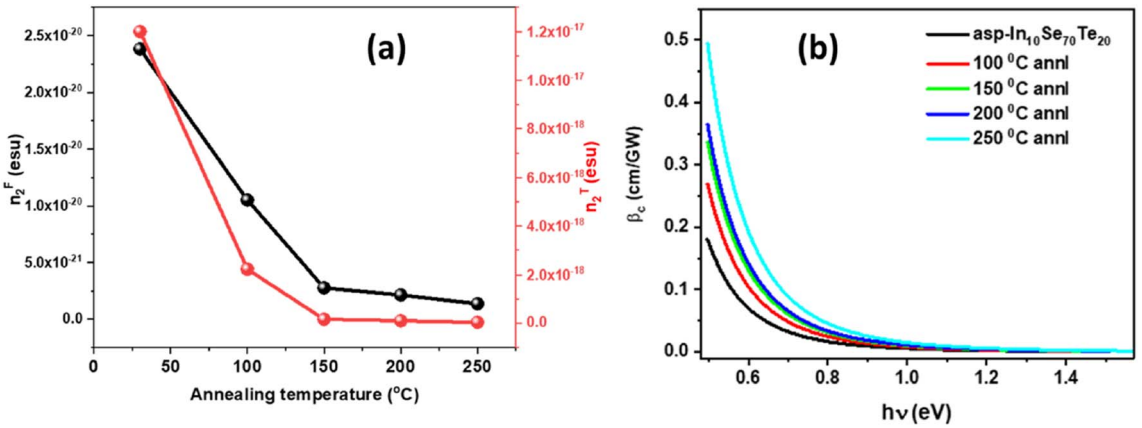

Fig. 12 (a) Variation in n_2^F and n_2^T and (b) β_c with energy in $In_{10}Se_{70}Te_{20}$ thin films.

where $E(t)$ and ε_0 are the electric field strength and permeability in free space. Electrical susceptibility has linear susceptibility (χ^1) and non-linear susceptibility (χ^2, χ^3). The materials with inversion symmetry have the even order terms as zero for the non-linear susceptibility *i.e.* $\chi^2 = 0$. The linear susceptibility χ^1 is given by the following formula:[88]

$$\chi^1 = \frac{{n_0}^2 - 1}{4\pi} \tag{17b}$$

where 'n_o' is the linear refractive index. The values of χ^1 are presented in Table 2, which shows the decreased value with annealing of $In_{10}Se_{70}Te_{20}$ films. Miller's generalised rule[88] was used to obtain third-order non-linear optical susceptibility (χ^{13}):

$$\chi^{(3)} = A(\chi^{(1)})^4 \tag{17c}$$

where A is 1.7×10^{-10} esu. The values of $\chi^{(3)}$ for different annealed films are listed in Table 2, which also decreases with annealing. The polarized atoms with lone pairs (chalcogens) affect χ^3 value, but the presence of heavy atoms with easily polarized electron clouds (*e.g.* In) is even more suitable. This monotonic decrease in non-linear susceptibility is caused by a change in material structure caused by annealing-induced enhancement in crystallization and crystallite size.

The nonlinear refractive index is calculated from $\chi^{(3)}$ using the Tichy and Ticha formula:[88]

$$n_2^T = \frac{12\pi\chi^{(3)}}{n_0}. \tag{17d}$$

The value of n_2^T is found to decrease with the annealing of $In_{10}Se_{70}Te_{20}$ films, as shown in Table 2. The n_2^T value for the as-prepared $In_{10}Se_{70}Te_{20}$ film decreased from 1.2×10^{-17} esu to 4.15×10^{-20} esu for 250 °C annealing. Fornier and Snitzer correlated the n_2^F and linear refractive index of the material using WDD parameters as follows:[89]

$$n_2^F = \frac{(n^2+2)(n^2-1)}{48\pi\ Nn}\ \frac{E_d}{(E_0)^2}\left(\frac{{x_{32}}^2}{{x_{2g}}^2} - 1\right), \tag{17e}$$

where n is the refractive index, N is the density of polarizable constituents, and subscripts g, 2 and 3 to x denote the ground state (g) and excited states (2 and 3), respectively. Considering the three-level system for this model, the quantity $(({x_{32}}^2/{x_{2g}}^2) - 1) = 1$ and n as static refractive index n_o, the above equation becomes[89]

$$n_2^F = \frac{({n_0}^2+2)({n_0}^2-1)}{48\pi N n_0}\ \frac{E_d}{(E_0)^2}. \tag{17f}$$

The estimated $n_2{}^F$ using the Fornier and Snitzer models is presented in Table 2. The n_2^F showed a lower value compared to n_2^T. The comparative plot presented in Fig. 12a showed that both n_2^F and n_2^T follow the same trend as that of the linear refractive index, *i.e.*, overall decreased with an increase in annealing temperature. Furthermore, the change in E_g, χ^3 and n_2 under different annealing conditions is shown in Fig. S4.† The number of homopolar bonds decreased with an increase in heteropolar ones, thus decreasing the defects in the band structure. Therefore, the reduction in the density of defects and the decrease in the variety of defects account for the decrease in non-linearity with annealing. Lowering of $\chi^{(3)}$ and n_2 upon annealing is suitable for solid-state laser and UV non-linear materials.[90]

Two-photon absorption (TPA) is one of the most fundamental mechanisms that describes the procedure of induced absorption inside materials. This mechanism happens only when the energy of incident light is in the range of $E_g/2 < h\nu < E_g$. This TPA mechanism is described by the non-linear absorption coefficient (β_c), which can be calculated using a simple empirical relation by Sheik Bahae *et al.*:[75,91,92]

$$\beta_c(\nu) = \frac{3100\ \sqrt{21}\left[\left(\frac{2h\nu}{E_g}\right) - 1\right]^{\frac{3}{2}}}{n^2 {E_g}^3\left[\frac{2h\nu}{E_g}\right]^5}\text{cm GW}^{-1}. \tag{17g}$$

The β_c value showed greater magnitude at a lower energy and was then reduced. Fig. 12b shows the same pattern of β_c as the

non-linear parameters, *i.e.*, increased with annealing temperature.

4. Conclusions

The findings from this study showed that annealing induced an increase in crystallinity and a decrease in dislocation density in $In_{10}Se_{70}Te_{20}$ thin films. The particle size increased from 9.55 nm of the as-deposited one to 18.68 nm for the 250 °C annealed film. The structural change is due to the annealing out of the unsaturated bonds and defects in the film with heat energy, increasing the structural order. The In_2Se_3 and In_2Te_3 phase formation from the $In_{10}Se_{70}Te_{20}$ film was confirmed by XRD and Raman studies. Surface morphological modification was noticed from the FESEM images, and the elemental mapping study showed a uniform distribution of elements in the film. The indirect allowed bandgap is found to be increased by 0.227 eV for the 250 °C annealed film from the as-deposited one. Such an increase in E_g is due to the increase in crystallinity and decrease in defects caused by annealing. The steepness parameter increased, and the S_{e-p} value decreased with annealing. The effect of annealing temperature is observed on the dispersion and the non-linear parameters. The 'k' and 'α' values decreased by making the film more transparent upon annealing. The decrease in refractive index satisfies the Moss rule and results in an increase in E_o value by 0.073 eV and a decrease in E_d value by 0.0881 eV due to annealing. The oscillator strength, first and third moments of spectra, dielectric constant carrier concentration and oscillator wavelength decreased upon annealing. Simultaneously, plasma frequency increased from 8.67 to 9.65, and optical electronegativity increased with annealing temperature. Electrical susceptibility decreased along with optical conductivity. The non-linear refractive index decreased from 1.2×10^{-17} esu (as-prepared) to 4.15×10^{-20} esu (250 °C), as did the non-linear susceptibility with annealing. The observed changes in the linear and non-linear optical parameters with annealing temperature are suitable for optoelectronic and non-linear optics.

Author contributions

S. Giri: writing – original draft, software, data curation, investigation. P. Priyadarshini: experiment, data curation. D. Alagarasan: experiment, investigation. R. Ganesan: visualisation, investigation. R. Naik: conceptualization, methodology, writing – review & editing, supervision.

Data availability

The data that support the findings of this study are available from the corresponding author upon reasonable request.

Conflicts of interest

There are no conflicts of interest for this manuscript.

Acknowledgements

R. Naik thanks ICT-IOCB for the Central Instrument facility.

References

1 M. H. R. Lankhorst, B. W. S. M. M. Ketelaars and R. A. M. Wolters, Low-cost and nanoscale and non-volatile memory concept for future silicon chips, *Nat. Mater.*, 2005, **4**, 347–352.
2 C. Tan, M. Amani, C. Zhao, M. Hettick, X. Song, D. H. Lien, H. Li, M. Yeh, V. R. Shrestha, K. B. Crozier, M. C. Scott and A. Javey, Evaporated Se_xTe_{1-x} Thin films with tunable bandgaps for short-wave infrared photodetectors, *Adv. Mater.*, 2020, **32**, 2001329.
3 A. Rawat, A. Arora and A. De Sarkar, Interfacing 2D M_2X (M= Na, K, Cs; X= O, S, Se, Te) monolayers for 2D excitonic and tandem solar cells, *Appl. Surf. Sci.*, 2021, **563**, 150304.
4 E. Colegrove, B. Good, A. Abbas, H. Moutinho, S. Johnston, C.-S. Jiang, P. O'Keefe, J. M. Walls, D. S. Albin and M. O. Reese, Investigating the role of copper in arsenic doped Cd (Se, Te) photovoltaics, *Sol. Energy Mater. Sol. Cells*, 2022, **246**, 111886.
5 S. Maurugeon, B. Bureau, C. Boussard-Pledel, A. J. Faber, P. Lucas, X. H. Zhang and J. Lucas, Selenium modified $GeTe_4$ based glasses optical fibers for far-infrared sensing, *Opt. Mater.*, 2011, **33**, 660–663.
6 I. Pethes, R. Chahal, V. Nazabal, C. Prestipino, A. Trapananti and S. Michalik, Chemical short-range order in selenide and telluride glasses, *J. Phys. Chem. B*, 2016, **120**, 9204.
7 S. Cui, R. Chahal, C. Boussard-Pledel, V. Nazabal, J. L. Doualan, J. Troles, J. Lucas and B. Bureau, From selenium- to tellurium-based glass optical fibers for infrared spectroscopies, *Molecules*, 2013, **18**, 5373–5388.
8 Y. Sung-Min, L. Nam-Yeal, R. Sang-Ouk, C. Kyu-Jeong, Y. S. Park, L. Seung-Yun, Y. Byoung-Gon, K. Myung-Jin, C. Se-Young and M. Wuttig, Sb–Se-based phase-change memory device with lower power and higher speed operations, *IEEE Electron Device Lett.*, 2006, **27**, 445–447.
9 Y. Lu, S. Song, X. Shen, L. Wu, Z. Song, B. Liu, S. Dai and Q. Nie, Investigation of $Ga_8Sb_{34}Se_{58}$ material for low-power phase change memory, *ECS Solid State Lett.*, 2013, **2**, 94–96.
10 R. Svoboda, M. Kincl and J. Malek, Thermal characterization of Se–Te thin films, *J. Alloys Compd.*, 2015, **644**, 40–46.
11 A. Zakery and S. R. Elliott, Optical properties and applications of chalcogenide glasses: a review, *J. Non-Cryst. Solids*, 2003, **330**, 1–12.
12 A. A. Wilhelm, C. B. Pledel, Q. Coulombier, J. Lucas, B. Bureau and aP. Lucas, Development of far-infrared-transmitting Te based glasses suitable for carbon dioxide detection and space optics, *Adv. Mater.*, 2007, **19**, 3796–3800.
13 S. Raoux, W. Welnic and D. Ielmini, Phase change materials and their application to nonvolatile memories, *Chem. Rev.*, 2010, **110**, 240–267.
14 M. Wuttig and C. Steimer, Phase change materials: from material science to novel storage devices, *Appl. Phys. A*, 2007, **87**, 411–417.

15 M. Wuttig and N. Yamada, Phase-change materials for rewriteable data storage, *Nat. Mater.*, 2007, **6**, 824–832.
16 W. Welnic, J. A. Kalb and D. Wamwangi, Phase change materials: from structures to kinetics, *J. Mater. Res.*, 2007, **22**, 2368–2375.
17 S. O. Kasap, T. Wagner, V. Aiyah, O. Krylouk, A. Bekirov and L. Tichy, Amorphous chalcogenide Se_{1-x-y} Te_xP_y semiconducting alloys: thermal and mechanical properties, *J. Mater. Sci.*, 1999, **34**, 3779–3787.
18 A. Kumar, M. Lal, K. Sharma, S. K. Tripathi and N. Goyal, Electrical properties of $Se_{85-x}Te_{15}$ In_x, *Chalcogenide Lett.*, 2012, **9**, 275–285.
19 J. Sanghera, I. Aggarwal, L. Busse, P. Pureza, V. Nguyen, R. Miklos, F. Kung and R. Mossadegh, Development of low loss IR transmitting chalcogenide glass fibers, *Proc. SPIE*, 1995, **2396**, 71.
20 E. O. Wrasse, A. Torres, R. J. Baierle, A. Fazzio and T. M. Schmidt, Size effects induced high thermoelectric figure of merit in PbSe and PbTe nanowires, *Phys. Chem. Chem. Phys.*, 2014, **16**, 8114–8118.
21 E. A. Banik and K. Biswas, Lead-free thermoelectrics: Promising thermoelectric performance in p-type $SnTe_{1-x}Se_x$ system, *J. Mater. Chem. A*, 2014, **2**, 9620–9625.
22 J. Zhen, W. Deng, C. Li, J. Feng, S. Zhang, S. Wan, G. Wang, H. Dong, R. A. Susilo and B. Chen, Superconductivity in In_2Te_3 under compression induced by electronic and structural phase transitions, *J. Phys. Chem. Lett.*, 2022, **13**, 1226–1233.
23 J. Yao, Z. Deng, Z. Zheng and G. Yang, Stable, Fast UV–Vis–NIR photodetector with excellent responsivity, detectivity, and sensitivity based on α-In_2Te_3 films with a direct bandgap, *ACS Appl. Mater. Interfaces*, 2016, **8**, 20872–20879.
24 V. Sowjanya, K. V. Bangera and G. K. Shivakumar, Structural, electrical and optical properties of stoichiometric In_2Te_3 thin films, *Ceram. Int.*, 2017, **43**, 3748–3751.
25 N. Guettari, C. Amory, M. Morsli, J. C. Bernede and A. Khelil, In_xTe_y semiconductor thin films obtained by co-evaporation, *Thin Solid Films*, 2003, **431–442**, 497–501.
26 Y. T. Huang, N. K. Chen, Z. Z. Li, X. P. Wang, H. B. Sun, S. Zhang and X. B. Li, Two-dimensional In_2Se_3: A rising advanced material for ferroelectric data storage, *Info Mat.*, 2022, **4**, 2341.
27 L. Wang, X. Wang, Y. Zhang, R. Li, T. Ma, K. Leng, Z. Chen, I. Abdelwahab and K. P. Loh, Exploring ferroelectric switching in α-In_2Se_3 for neuromorphic computing, *Adv. Funct. Mater.*, 2020, **30**, 2004609.
28 G. Almeida, S. Dogan, G. Bertoni, C. Giannini, R. Gaspari, S. Perissinotto, R. Krahne, S. Ghosh and L. Manna, Colloidal monolayer β-In2Se3 nanosheets with high photoresponsivity, *J. Am. Chem. Soc.*, 2017, **139**, 3005–3011.
29 W. Zheng, T. Xie, Y. Zhou, Y. L. Chen, W. Jiang, S. Zhao, J. Wu, Y. Jing, Y. Wu, G. Chen, Y. Guo, J. Yin, S. Huang, H. Q. Xu, Z. Liu and H. Peng, Patterning two-dimensional chalcogenide crystals of Bi_2Se_3 and In_2Se_3 and efficient photodetectors, *Nat. Commun.*, 2015, **6**, 6972.
30 S. R. Herd, K. Y. Ahn, R. J. Von Gutfeld and D. R. Vigliotti, Structural changes in Se-Te bilayers by laser writing, *J. Appl. Phys.*, 1982, **53**, 5.
31 S. M. Elkatlawy, A. H. El-Dosokey and H. M. Gomaa, Structural properties, linear, and non-linear optical parameters of ternary $Se_{80}Te_{(20-x)}$ In_x chalcogenide glass systems, *Bol. Soc. Esp. Ceram. Vidrio*, 2020, **61**, 203–209.
32 N. S. Saxena, M. M. Imran and K. Singh, Simultaneous measurements of thermal conductivity and diffusivity of $Se_{80}Te_{20-x}In_x$ (x = 2, 4, 6 and 10) chalcogenide glasses at room temperature, *Bull. Mater. Sci.*, 2002, **25**, 241–245.
33 V. Sharma, A. Thakur, N. Goyal, G. Saini and S. Tripathi, Effect of In additive on the electrical properties of Se–Te alloy, *Semicond. Sci. Technol.*, 2004, **20**, 103.
34 T. Akiyama, M. Uno, H. Kitaura, K. Narumi, R. Kojima and K. Nishiuchi, Rewritable dual-layer phase-change optical disk utilizing a blue-violet laser, *Jpn. J. Appl. Phys.*, 2001, **40**, 1598.
35 P. Priyadarshini, D. Sahoo, D. Alagarasan, R. Ganesan, S. Varadharajaperumal and R. Naik, Structural and optoelectronic properties change in Bi/In2Se3 heterostructure films by thermal annealing and laser irradiation, *J. Appl. Phys.*, 2021, **129**, 223101–223111.
36 R. Panda, S. A. Khan, U. P. Singh, R. Naik and N. C. Mishra, The impact of fluence dependent 120 MeV Ag swift heavy ion irradiation on the changes in structural, electronic, and optical properties of $AgInSe_2$ nano-crystalline thin films for optoelectronic applications, *RSC Adv.*, 2021, **11**, 26218–26227.
37 R. Panda, M. Panda, H. Rath, U. P. Singh, R. Naik and N. C. Mishra, annealing induced AgInSe2 formation from Ag/In/Ag/In multilayer film for solar cell absorbing layer, *Opt. Mater.*, 2018, **84**, 618–624.
38 D. Sahoo, S. Sahoo, D. Alagarasan, R. Ganesan, S. Varadharajaperumal and R. Naik, Proton ion irradiation on As40Se50Sb10 thin films: Fluence-dependent tuning of linear–Non-linear optical properties for photonic applications, *ACS Appl. Electron. Mater.*, 2022, **4**, 856–868.
39 R. Panda, R. Naik and N. C. Mishra, Low-temperature growth of γ phase in thermally deposited In_2Se_3 thin films, *Phase Trans.*, 2019, **91**, 862–871.
40 H. P. Pathak, N. Shukla, V. Kumar and D. K. Dwivedi, Structural and optical properties of In doped Se–Te phase-change thin films: a material for optical data storage, *Opt. Mater.*, 2016, **52**, 69–74.
41 Y. H. Abdelalim, A. H. A. Sakr, S. M. El-Ghanam and M. A. Hamad, Tailoring of optical properties of $Se_{80}Te_{20-x}In_x$ films by annealing process, *Appl. Phys. A*, 2022, **128**, 643.
42 A. M. Abd-Elnaiem, S. Moustafa, A. M. Abdelraheem, M. A. Abdel-Rahim and A. Z. Mahmoud, Effects of Annealing on structural and optical properties of $Ge_{20}Se_{70}Sn_{10}$ thin films for optoelectronic applications, *J. Non-Cryst. Solids*, 2020, **549**, 120353.
43 M. Rashad, R. Amin, S. A. Al-Ghamdi, M. M. Hafiz and A. M. Abd-Elnaiem, Improving the electrical parameters of $Se_{80}Te_{20}$ films by the Sn substitution for Te and thermal-induced effect, *J. Electron. Mater.*, 2021, **50**, 2075–2082.

44 H. Sing, S. Kumari, P. Singh, A. Kumar and A. Thakur, Effect of Annealing on structural, morphological and optical properties of InSe thin films, *J. Mater. Sci.: Mater. Electron.*, 2022, **33**, 23599–23606.

45 A. Parida, D. Sahoo, D. Alagarasan, S. Vardhrajperumal, R. Ganesan and R. Naik, Increase in non-linear susceptibility and refractive index in quaternary $In_{15}Sb_{10}S_{15}Se_{60}$ thin films upon annealing at different temperature for photonic applications, *J. Alloys Compd.*, 2022, **905**, 164143.

46 S. Das, S. Senapati, D. Alagarasan, S. Vardhrajperumal, R. Ganesan and R. Naik, Enhancement of non-linear optical parameters upon phase transition in new quaternary $Ge_{20}Ag_{10}Te_{10}Se_{60}$ films by annealing at various temperatures for optoelectronic applications, *J. Alloys Compd.*, 2022, **927**, 167000.

47 S. Sharma, R. Sharma, P. Kumar, R. Thangaraj, K. Ashokan and M. Mian, Structural, optical and photoelectrical properties of thermally annealed amorphous $In_{15}Sb_{15}Se_{70}$ chalcogenide films, *Appl. Phys. A*, 2018, **124**, 357.

48 A. Harizia, M. B. Rabeha, F. Laatarb, F. C. Akkaria and M. Kanzaria, Substrate temperature dependence of structural, morphological and optical properties of $Sn_4Sb_6S_{13}$ thin films deposited by vacuum thermal evaporation, *Mater. Res. Bull.*, 2016, **79**, 52–62.

49 P. Priyadarshini, S. Das, D. Algarasan, R. Ganesan, S. Varadharajaperumal and R. Naik, Role of Bismuth incorporation on the structural and optical properties in Bi_xIn_{35}-xSe_{65} thin films for photonic applications, *J. Am. Ceram. Soc.*, 2021, **104**, 5803–5814.

50 J. Weszka, Ph. Daniel, A. Burian, A. M. Burian and A. T. Nguyen, Raman scattering in In_2Se_3 and $InSe_2$ amorphous, *J. Non-Cryst. Solids*, 2000, **265**, 98–104.

51 C. H. Ho, Amorphous effect on the advancing of wide-range absorption and structural-phase transition in γ-In_2Se_3 polycrystalline layers, *Sci. Rep.*, 2014, **4**, 4764.

52 S. Das, P. Priyadarshini, D. Alagarasan, S. Vardhrajperumal, R. Ganesan and R. Naik, Structural, morphological, and linear/non-linear optical properties tuning in Ag_{60}-$xSe_{40}Te_x$ films by thermal annealing for optoelectronics, *J. Non-Cryst. Solids*, 2022, **592**, 121742.

53 I. Childres, J. Tian, I. Mitokowski and Y. Chen, AFM and Raman studies of topological insulator materials subject to argon plasma etching, *Philos. Mag.*, 2013, **93**, 681–689.

54 G. Abbady, A. Qasem and A. M. Abd-Elnaiem, Optical parameters and electronic properties for the transition of the amorphous-crystalline phase in $Ge_{20}Te_{80}$ thin films, *J. Alloys Compd.*, 2020, **842**, 155705.

55 A. M. Adam, E. Lilov, V. Lilova and P. Petkov, Characterization and optical properties of bismuth chalcogenide films prepared by pulsed laser deposition technique, *Mater. Sci. Semicond. Process.*, 2017, **57**, 210–219.

56 D. Sahoo, P. Priyadarshini, A. Aparimita, D. Alagarasan, R. Ganesan, S. Varadharajaperumal and R. Naik, Role of annealing temperature on optimizing the linear and non-linear optical properties of As40Se50Ge10 films, *RSC Adv.*, 2020, **10**, 26675–26685.

57 H. Nyakotyo, T. S. Sathiaraj and E. Muchuweni, Effect of Annealing on the optical properties of amorphous $Se_{79}Te_{10}Sb_4Bi_7$ thin films, *Opt. Laser Technol.*, 2017, **92**, 182–188.

58 R. K. Pan, H. Z. Tao, H. C. Zang, X. J. Zhao and T. J Zhang, Annealing effects on the structure and optical properties of GeSe2 and GeSe4 films prepared by PLD, *J. Alloys Compd.*, 2009, **484**, 645.

59 S. Mishra, P. K. Singh, P. Lohia and D. K. Dwivedi, Thin film preparation and optical properties of Se–Te based chalcogenide glasses for optoelectronic applications, *Glass Phys. Chem.*, 2020, **46**, 341–349.

60 A. A. A. Darwish and H. A. M. Ali, On annealing induced effect in optical properties of amorphous GeSeSn chalcogenide films for optoelectronic applications, *J. Alloys Compd.*, 2017, **710**, 431–435.

61 A. A. Al-Ghamdi, S. A. Khan, S. Al-Heniti, F. A. Al-Agel and M. Zulfequar, Effects of laser irradiation on optical properties of amorphous and annealed $Ga_{15}Se_{81}In_4$ and $Ga_{15}Se_{79}In_6$ chalcogenide thin films, *J. Alloys Compd.*, 2010, **505**, 229–234.

62 A. A. Al-Ghamdi, S. A. Khan, S. Al-Heniti, F. A. Al-Agel and M. Zulfequar, Annealing and laser irradiation effects on optical constants of $Ga_{15}Se_{85}$ and $Ga_{15}Se_{83}In_2$ chalcogenide thin films, *Curr. Appl. Phys.*, 2011, **11**, 315–320.

63 A. Parida, D. Sahoo, D. Alagarasan, S. Varadharajaperumal, R. Ganesan and R. Naik, Impact on non-linear/linear optical and structural parameters in quaternary $In_{15}Ag_{10}S_{15}Se_{60}$ thin films upon annealing at different temperatures, *Ceram. Int.*, 2022, **48**, 15380–15389.

64 P. Priyadarshini, S. Das, D. Alagarasan, R. Ganesan, S. Varadharajaperumal and R. Naik, Annealing induced modification in linear and non-linear optical properties of $Bi_7In_{28}Se_{65}$ thin films for non-linear applications, *Opt. Mater.*, 2021, **122**, 111801.

65 A. S. Hassanien and I. Sharma, Band-gap engineering, conduction and valence band positions of thermally evaporated amorphous $Ge_{15-x}Sb_xSe_{50}Te_{35}$ thin films: Influences of Sb upon some optical characterizations and physical parameters, *J. Alloys Compd.*, 2019, **798**, 750–763.

66 J. Tauc and A. Menth, States in the gap, *J. Non-Cryst. Solids*, 1972, **8**, 569–585.

67 N. F. Mott and E. A. Davis, *Electronic Processes in Non-Crystalline Materials*, Clarendon Press, Oxford, 1979, p. 210.

68 A. El-Korashy, A. Bakry, M. A. Abdel-Rahim and M. Abd El-Sattar, Annealing effects on some physical properties of $Ge_5Se_{25}Te_{70}$ chalcogenide glasses, *Phys. B*, 2007, **391**, 266–273.

69 K. A. Aly, N. Afify, A. M. Abousehlly and A. M. Abd Elnaeim, Optical band gap and refractive index dispersion parameters of In–Se–Te amorphous films, *J. Non-Cryst. Solids*, 2011, **357**, 2029–2034.

70 S. Das, P. Priyadarshini, D. Alagarasan, S. Vardhrajperumal, R. Ganesan and R. Naik, Role of tellurium addition on the linear and non-linear optical, structural, morphological properties of $Ag_{60-x}Se_{40}Te_x$ thin films for non-linear applications, *J. Am. Ceram. Soc.*, 2022, **105**, 3469–3484.

71 S. Agarwal, P. Lohia and D. K. Dwivedi, Emerging phase change memory devices using non-oxide semiconducting glasses, *J. Non-Cryst. Solids*, 2022, **597**, 121874.
72 R. K. Pan, H. Z. Tao, H. C. Zang, X. J. Zhao and T. J. Zhang, Annealing effects on the structure and optical properties of $GeSe_2$ and $GeSe_4$ films prepared by PLD, *J. Alloys Compd.*, 2009, **484**, 645.
73 C. Liu, Y. K. Kwon and J. Hao, Absorption and photoluminescence of PbS QDs in glasses, *J. Non-Cryst. Solids*, 2009, **355**, 1880–1883.
74 F. Gami, I. Guizani, M. A. Sebak, A. A. Abuelwafa and M. M. Mostafa, Investigation of structural, optical and electrical properties of PCBM/ZnOEP thin films, *Opt. Mater.*, 2022, **134**, 113093.
75 S. Agarwal, P. Lohia and D. K. Dwivedi, Study of optical parameters of $Te_{(1-x)}$ $(GeSe_{0.5})$ Sc_x $(0 \leq x \leq 0.15)$ thin films for optical data storage applications, *J. Non-Cryst. Solids*, 2023, **606**, 122199.
76 M. Dongol, A. F. Elhady, M. S. Ebied and A. A. Abuelwafa, Effect of thermal Annealing on the optical properties of $Ge_{20}Se_{65}S_{15}$ thin films, *Ind. J. Phys.*, 2021, **95**, 1245–1253.
77 A. Srivastava, S. N. Tiwari and M. A. Alvi, Phase change studies in $Se_{85}In_{15-x}Zn_x$ chalcogenide thin films, *J. Appl. Phys.*, 2018, **123**, 125105.
78 F. Urbach, The long-wavelength edge of photographic sensitivity and of the electronic absorption of solids, *Phys. Rev.*, 1953, **92**, 1324.
79 S. Yaseem, F. Iqbal, T. Munawar, M. A. Nawaz, M. Asghar and A. Hussain, Synthesis, structural and optical analysis of surfactant assisted ZnO–NiO nanocomposites prepared by homogeneous precipitation method, *Ceram. Int.*, 2019, **45**, 17859–17873.
80 I. Sharma, S. K. Tripathi and P. B. Barman, Effect of Bi addition on the optical behavior of a-Ge-Se-In-Bi thin films, *Appl. Surf. Sci.*, 2008, **255**, 2791–2795.
81 T. S. Moss, A relationship between the refractive index and the infra-red threshold of sensitivity for photoconductors, *Proc. Phys. Soc., London, Sect. B*, 1950, **63**, 167–176.
82 A. S. Hassanien and A. A. Akl, Optical characterizations and refractive index dispersion parameters of annealed TiO2 thin films synthesized by RF-sputtering technique at different flow rates of the reactive oxygen gas, *Phys. B*, 2020, **576**, 411718.
83 A. El-Denglawey, M. Makhlouf and M. Dongol, The effect of thickness on the structural and optical properties of nano Ge-Te-Cu films, *Res. Phys.*, 2018, **10**, 714–720.
84 A. Bute, S. Jena, R. Sharma, D. Udupa and N. Maiti, Linear and non-linear optical properties of boron carbide thin films, *Appl. Surf. Sci.*, 2023, **608**, 155101.
85 A. S. Hassanien and I. Sharma, Optical properties of quaternary a-$Ge_{15-x}Sb_xSe_{50}Te_{35}$ thermally evaporated thin-films: refractive index dispersion and single oscillator parameters, *Optik*, 2020, **200**, 163415.
86 A. S. Hassanien and I. Sharma, Dielectric properties, Optoelectrical parameters and electronic polarizability of thermally evaporated a-Pb-Se-Ge thin films, *Phys. B*, 2021, **622**, 413330.
87 D. Sahoo, D. Alagarasan, R. Ganesan, S. Varadharajaperumal and R. Naik, Impact of irradiation doses on the structural, morphological, and linear-nonlinear optical properties of $Ge_{10}Sb_{25}Se_{65}$ thin films for optoelectronic applications, *Eur. Phys. J. Plus*, 2022, **137**, 707.
88 L. Tichý, H. Ticha, P. Nagels, R. Callaerts, R. Mertens and M. Vlcek, Optical properties of amorphous As-Se and Ge-As-Se thin films, *Mater. Lett.*, 1999, **39**, 122–128.
89 S. Mishra, P. K. Singh, R. K. Yadav, A. Kumar, P. Lohia and D. K. Dwivedi, Investigation of glass forming ability, linear and non-linear optical properties of Ge-Se-Te-Sb thin films, *Chem. Phys.*, 2021, **541**, 111021.
90 X. Dong, L. Huang, Q. Liu, H. Zeng, Z. Lin, D. Xu and G. Zou, Perfect balance harmony in $Ba_2NO_3(OH)_3$: a beryllium-free nitrate as a UV non-linear optical material, *Chem. Commun.*, 2018, **54**, 5792–5795.
91 A. A. Abuelwafa, M. S. Abd El- sadek, S. Elnobi and T. Soga, Effect of transparent conducting substrates on the structure and optical properties of tin (II) oxide (SnO) thin films: Comparative study, *Ceram. Int.*, 2021, **47**, 13510–13518.
92 A. A. Abuelwafa, H. M. Alsoghier, S. Elnobi, M. Dongol and T. Soga, Quantum computational, linear and non-linear optical properties of spin-coated nickel (II)-tetraphenylporphyrin/FTO thin films, *Optik*, 2021, **234**, 166618.